FACULTY OF SCIENCE AND TECHNOLOGY

MASTER THESIS

Study programme / specialisation:
Mechanical and Structural Engineering and
Materials Science / Renewable Energy

The spring semester, 2022

Open / Confidential

Author: Usman Shaukat

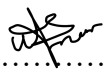

……
(signature author)

Course coordinator: Knut Erik Teigen Giljarhus

Supervisor: Knut Erik Teigen Giljarhus

Thesis title: Investigation of smoothing in the actuator line model for single and multi-rotor wind turbines

Credits (ECTS): 30

Keywords: *wind turbine, actuator line modeling, multi-rotor, single rotor, Gaussian radius, large-eddy simulations, NTNU model wind turbine, MEXICO Rotor, equivalent elliptic planform, OpenFOAM, turbinesFOAM*

Pages: 69

Stavanger, 15/06/2022

ABSTRACT

The state-of-the-art actuator line modeling (ALM) method has been used extensively in the past decade to perform large-eddy simulations (LES) of wind turbines as fully resolved blade simulations require complex rotating meshes and are computationally expensive. The ALM method represents rotor blades as the line of the elements. Each element actuates forces that are projected onto the flow field as a body force using volumetric projection. Thus, the thesis mainly focuses on smoothing the radius of actuator force projection along the blade span because the rotor power and blade tip loading are susceptible to this ALM parameter. The commonly used constant chord and grid sizes method for the volumetric force projection radius overpredicts the blade tip loading on the wind turbine. As a result, the researcher developed the elliptic distribution method to improve the prediction of blade tip loading, but it has not been used extensively. Therefore, these three methods are applied to the NTNU model wind turbine and the MEXICO rotor to prove their validity. The NTNU model wind turbine has a smaller size and aspect ratio than the MEXICO rotor. The results showed that the elliptic chord distribution method on the NTNU wind turbine gave a better power and blade tip loading prediction than the constant chord and grid-based Gaussian radius method. However, the three Gaussian radius methods gave the same results for the power and blade tip loadings prediction on the MEXICO rotor. The time step and grid size selection for LES-ALM simulation have also been discussed. The recent shift towards the multi-rotor concept has been observed in the offshore wind turbine industry as it can potentially decrease the levelized cost of energy due to its smaller components which are easier to handle. Hence, the second part of the thesis measures the aerodynamic performance of the multi-rotor system in comparison to the single rotor. The ALM results showed an increase in individual rotor power and blade loading by 4% and 2%, respectively, for multi-rotor compared to the single rotor. In addition, less velocity deficit is observed for the two rotors compared to the single rotor.

Keywords: *wind turbine, actuator line modeling, multi-rotor, single rotor, Gaussian radius, large-eddy simulations, NTNU model wind turbine, MEXICO Rotor, equivalent elliptic planform, OpenFOAM, turbinesFOAM*

ACKNOWLEDGEMENT

The thesis became a reality because of the individuals I met in my life who shared their knowledge with me. Foremost, I would like to sincerely thank my supervisor, Associate Professor Knut Erik Teigen Giljarhus, for countless support and for providing me with every possible assistance in completing this thesis. His guidance has helped me throughout the research and writing of the thesis.

Besides my professor, I owe a debt of gratitude to my family, my parents, Robina Kausar and Shaukat Mahmood, for raising, teaching, and supporting me throughout my life, my sisters Mehreen Shaukat and Sehrish Shaukat, and my brother Sulman Shaukat for being the best siblings and giving me the best life experience, and motivating me throughout my life journey.

Last but not least, I would like to thank my peers, Cristina Tawede Besin and Navaneethan Kurukkal, for the stimulating conversations and all the fun we have had together during this two-year journey. I would also like to thank my friends, Hassan Abdullah, Raja Musa, and Abdullah Massod, in Pakistan; this could not be possible without them.

TABLE OF CONTENTS

LIST OF FIGURES

LIST OF FIGURES

LIST OF TABLES

LIST OF ABBREVIATIONS

ACE	Actuator Curve Embedding
ADM	Actuator Disk Model
ALM	Actuator Line Model
AR	Aspect Ratio
BEM	Blade Element Momentum
CFD	Computational Fluid Dynamics
HAWT	Horizontal Axis Wind Turbine
LES	Large Eddy Simulation
LCOE	Levelized cost of energy
MRF	Multireference Frame
NREL	National Renewable Energy Laboratory
RANS	Reynolds-Averaged Navier-Stokes
SGS	Sub Grid Scale
SMI	Sliding Mesh Interface
TSR	Tip Speed Ratio
VAWT	Vertical Axis Wind Turbine
NTNU	Norwegian University of Science and Technology

LIST OF SYMBOLS

a	Axial induction factor
a'	Tangential induction factor
α	Angle of attack (deg)
A	Rotor area (m^2)
B	Number of turbine blades
c	Airfoil chord (m)
c^*	Equivalent elliptic chord (m)
C_d	Drag coefficient
C_l	Lift coefficient
C_n	Normal force coefficient
C_p	Power coefficient
C_s	Smagorinsky constant
C_T	Thrust coefficient
C_t	Tangential force coefficient
C_θ	Azimuthal velocity component in the wake
Δ_{grid}	Grid size (m)
Δ_p	Actuator width (m)
D	Diameter of Wind turbine (m)
$\boldsymbol{D}$	Strain rate tensor (s^{-1})
ε	Gaussian radius (m)
ϵ	Turbulent kinetic energy dissapation rate (m^2/s^3)
η	3D Gaussian distribution

LIST OF SYMBOLS

f_b	Actuator force (N)
F_d	Drag force (N)
F_d'	Drag force per unit length (N/m)
F_l	Lift force (N)
F_l'	Lift force per unit length (N/m)
F_n'	Normal/Axial force per unit length (N/m)
F_t'	Tangential force per unit length (N/m)
k	Turbulent kinetic energy (m^2/s^2)
λ	Tip speed ratio
$\lambda^{'}$	Local speed ratio
M	Torque (Nm)
Ma_{tip}	Mach number at the blade tip
v	Viscosity
ω	Wind turbine's angular velocity (s^{-1})
P	Turbine power (W)
ϕ	Flow angle (deg)
R	Turbine rotor radius (m)
r	Local radius (m)
ρ	Air density (kg/m^3)
σ	Solidity
T	Thrust force (N)
τ_{ij}	SGS stress tensor (N/m^2)
U	Wind Speed (m/s)
U_∞	Free Stream Wind (m/s)

CHAPTER 1 INTRODUCTION

The world's energy demand is growing exponentially due to the ever-increasing industrial developments. According to the International Energy Agency (IEA), the world's energy supply increased 65% from 1990 to 2019 [1]. In 2019, 82% of the energy came from conventional oil, coal, and gas sources. Due to the extreme reliance on energy from traditional sources, the CO_2 emissions have increased by 60% since the United Nations Framework Convention on Climate Change was signed in 1992. However, the Paris agreement signed in 2015 by the European Union country aims to achieve net-zero carbon greenhouse gas emissions by 2050 [2]. Therefore, steps have been taken to transition the energy supply to renewable energy sources such as solar and wind. As a result, the renewable energy shares in power generation increased to 23.5%, from which 11% is the energy generated from the wind in 2020 [3, 4]. The net-zero power generation level of 8 008 TWh in 2030 will require average wind generation growth of 18% per year during 2020-2030 and annual capacity additions of 310 GW of onshore wind and 80 GW of offshore wind [3]. Hence, harnessing wind energy with maximum efficiency is a primary challenge for engineers. According to the NREL data, the average life of an offshore wind farm is 25 years, and the cost of installing offshore wind energy worldwide averaged 3,185 U.S. dollars per kilowatt in 2021 [5]. Consequently, the short lifetime and high costs put the researcher at the vanguard of constantly improving the modeling techniques for better wind turbine design and power production prediction.

A wind turbine is a mechanical device that converts the wind's kinetic energy to mechanical energy and then electrical energy. Different wind turbines have been developed throughout history, but they can be classified into horizontal axis wind turbines (HAWT) and vertical axis wind turbines (VAWT). Wind turbines work on Bernoulli’s principle; the aerodynamic lift force generates over the wind turbine blades due to the difference in the pressure. Today, HAWTs are mostly part of the offshore and onshore wind farms since studies have shown that HAWTs provide a higher power coefficient than VAWTs. Therefore, for this thesis, HAWTs have been chosen for analysis.

In computational fluid dynamics (CFD), the full blade-resolved simulations of the wind turbine come at a high computational cost and prevent the simulation of the whole windfarms. As a result, the researchers have developed the actuator methods that can predict wind turbine power and wakes at an economical computational cost in CFD simulations. Therefore, the simulations of the actuator methods are between the low fidelity engineering simulations and the fully resolved bladed CFD simulations.

1.1 Literature Review of Actuator Line Modeling for Wind Turbine Simulations

Sorenson et al. [6], Leclerc et al. [7, 8], and Rathore et al. [9] developed the actuator disk model (ADM) for the RANS solvers to model the wind turbine based on the actuator disk theory by Glauert [10],. This method replaces the wind turbine rotor with the disk, and the disk actuates the force that introduces into the momentum equation of the flow solver. The drawback of this disk model is the lack of the blade details, tip vortices, and the blade's boundary layer, but it can predict the reasonable wake effects and can be used to model large wind farms. Therefore, there are still ongoing efforts made by Guodan Dong et al. [11], Revaz et al. [12], and Martinez-Tossas et al. [13] to model the wind turbine wake with the actuator disk model. However, the actuator disk model is limited to measuring far wake characteristics due to a lack of information about blades and tip vortices. Even for the multi-rotor system, the study is done only on the distant wake [14].

Due to the limitations mentioned earlier in ADM simulations, Sorensen and Shen [15] coined the Actuator Line Modelling (ALM) technique to model the wind turbines in 2002. It is a technique to predict the global flow fields around the wind turbine. In this concept, the blade loading implemented on the lines acting as blade rotor is introduced into the Navier-Stoke equations as the body force. The author stated the requirement of the two-dimensional airfoil data to determine corrected three-dimensional effects to limit the growth of the boundary layer due to the rotational impacts at separation, which can lead to an increased lift compared to two-dimensional characteristics. The force calculations were executed in a similar fashion to the Blade Element Momentum (BEM) approach. The results showed excellent validity with the measurements for the specific range of inflow velocities. Nevertheless, the method gave overprediction of power at

higher velocities. In the near wake, the vortices persisted for the only two turns and diffused to the continuous vortex sheet, contrary to the experiments that showed more number of turns. The author attributed this behavior to the low Reynolds number and the coarse grid downstream of the rotor. Moreover, the author mentioned two parameters (discussed in section 2.4) for calculating the actuator forces: velocity sampling and Gaussian radius or force smearing. However, the author did not correctly define the details for extracting the value for these two parameters, which led to the extensive research of these parameters in ALM simulations.

In the blind tests, Krogstad et al. [16] performed a series of simulations on the horizontal axis wind turbine model. The eleven different simulations were carried out using the method of BEM theory with LES using ALM and ADM methods. The measurements were made up to downstream of $X/D = 10$. The large-eddy simulations showed more reliable predictions than the other methods. The results were competitive with the blade resolved CFD. In addition, ALM-based LES simulations showed closer results than the actuator disk-based LES simulations, especially in the near wake region.

Archer et al. [17] performed the LES simulation of an entire wind farm using the state-of-the-art ALM technique. The six different configurations of the wind farm were studied. The actuator lines, consisting of 40 actuator points, are modeled to represent Siemens 2.3-MW wind turbine. The Gaussian projection radius was varied along the radial direction equal to chord length divided by a factor of 4.3. The 100,000 CPU-hours per run simulation results showed that staggering every second row increased the wind farm's capacity factor from 0.3 to 0.34. Increasing the wind turbine spacing and staggering every second row yielded the maximum capacity factor of 0.4 with the least amount of array losses of 14%.

The quantitative comparison between the RANS and LES-based simulations of wind farm modeled ALM technique was carried out by Tabib et al. [18]. The model consists of 25 wind turbines of $60\ m$ diameter on the geometrically resolved complex terrain, and the simulations were performed under neutral atmospheric conditions. The grid configuration was coarse, with the finest cells having a size of $6\ m$ in the turbine region leading to $\Delta_{grid}/R = 1/10$. The actuator line segment consists of 40 points leading to the actuator spacing of $\Delta_p/R = 1/40$. RANS simulations showed higher power predictions as compared to the LES solutions. As RANS shows quicker

wake recovery, the downstream turbines resulted in a higher power coefficient. The LES simulations showed that the placement of downstream turbines at four times the rotor diameter is not sufficient owing to wake interference.

The work of Troldborg [19] provided extensive guidelines for ALM simulations. The Ph.D. paper mentions the numerical parameters, such as the type of solver, the differencing scheme, and the time step required in ALM simulations. It also suggested the guideline for the optimum value of the Gaussian radius $\varepsilon = 2\Delta_{grid}$ that became the reference guide for the research. In addition, the study also showed that a minimum value of the projection radius ε resulted in the oscillation in the blade force distribution. The case with three turbines in a row is studied based on different inflow conditions. The laminar-based inflow showed stable tip vortices while wake was most visible in the turbulent flow case. All the turbines experienced the extreme tilt moment during the sheared inflow conditions, while the downstream turbines experienced yaw moments due to the wake generated by upstream turbines.

The work of Shives and Crawford [20] has made the breakthrough in determining the general guidelines needed for ALM parameters ε. Firstly, their study proposed the relation of Gaussian radius ε with the mesh spacing by performing the flow simulation on an infinite wing and the finite 3D wing with constant and elliptical circulation distributions. The results for the infinite wing simulations suggested that $\varepsilon/\Delta_{grid} \geq 4$ to avoid significant errors in computations. When they modeled the finite elliptic wing with the aspect ratio $AR = 10.2$ in RANS solver, their finding suggested that the Gaussian radius should vary in proportion to the local chord length c to predict the tip vortices accurately. At the same time, the grid spacing should be maintained to avoid numerical instability. The guidelines suggested the ratio ε/c should be approximately equal to the value of $1/8$ and $1/4$ to predict the downwash accurately. Their method is the first to predict the tip vortex without using any tip loss correction method.

Inspired by the work of Shives and Crawford [20], Jha et al. [21] proposed the guidelines to determine the ALM parameters: grid resolution Δ/R , Gaussian radius ε and for the LES simulations. Their finding suggested that the grid for the LES simulation should have an aspect ratio close to unity, and the time step should be selected such that the blades should not traverse more than one grid cell per time step. They tested three methods in defining the Gaussian radius ε

namely, the constant grid based $\varepsilon/\Delta_{grid}$, and constant chord based ε/c and proposed the new method based on elliptic planform distribution ε/c^* that accurately predict the tip vortices of the turbine blades on the two wind turbines having different aspect ratios: NREL-Phase IV rotor and NREL 5 MW. The results showed that the constant mesh-based Gaussian radius ε resulted in the over prediction of the tip vortices, while the constant chord-based Gaussian radius ε also shown a difference in the prediction of the blade loading but better results with regards to tip vortices. However, the elliptic planform distribution resulted in the closest agreement to the measured result for both wind turbines. The effects of the tip vortices are visible in the reduction of the blade loadings near the tip. The paper approximated the value for the maximum discretization criteria when defining the constant elliptic Gaussian radius ε/c^* and left it for future works for implementing it on other turbines for better approximation. In 2018, due to discrepancies present in the body-force distribution of the actuator line model, Jha et al. [22] published the new actuator curve embedding (ACE) concept. The ACE concept significantly improved predicting the spanwise force and tip vortices compared to the previous Gaussian radius concepts.

Schito and Zasso [23] studied the blade flow interaction using the actuator force approach to model the RANS and LES modeling in OpenFOAM. The study is done on the two-dimensional model, and the comparison is made between the results of the geometrically reproduced airfoil NACA0012 and the actuator force approach. The flow field showed the agreement only if a suitable regularization kernel (Gaussian radius) is applied; a small kernel ε results in too many numerical instabilities, while a large kernel ε cannot produce a near wake profile due to widely distributed forces. The epsilon ε value equal to the grid spacing Δ_{grid} is enough to accurately model the wakes.

Martinez-Tossas and Meneveau [24] have done the 2D potential flow analysis of the Joukowski airfoil to determine the optimal ALM parameters such as the location of the velocity sampling and gaussian radius ε for the finely resolved LES simulation having the grid spacing smaller than the chord length. The results showed that the optimal velocity sampling point should be at the center of the actuator force as it provides the correct point for the reference velocity due to the symmetric vorticity distribution. The optimal Gaussian radius ε should be 14% to 25% of the chord length c of the blade for the Joukowski airfoils. Since the value for optimum Gaussian radius of 25% is minimal, it also requires using very fine-scale large-eddy simulations. Therefore, the authors

developed a new sub-filter scale velocity model that uses a large value of Gaussian radius compared to the optimal value to simulate the coarse-scale large-eddy simulations [25]. Instead of Prandtl's original lifting line theory, which has an infinitesimally small vorticity source, the new model uses a new length scale for Gaussian radius ε at each blade section for vorticity distribution. When the epsilon's value goes to zero, the theory transforms to the original Prandtl's lifting line theory. This theory is tested in the LES flow simulation of the finite wing with constant and elliptic chord distribution, and the result shows agreement with the previous study of optimal chord length. However, the model suggested the assumption of neglecting the viscous and turbulence effect. The author justified that the lifting force on the wing depends on the pressure distribution compared to the viscosity and turbulence effect.

Evaluation of the ALM method on the coarser grids resolutions ($\Delta_{grid}/R = 1/8$ and $\Delta_{grid}/R = 1/15$), with a larger time step size than often recommended, has been done by Draper and Usera [26]. The simulations are performed on two wind turbines with TSR $\lambda = 6$ (upstream) and $\lambda = 4$ downstream. The ALM simulation of wind turbines that did not incorporate the tip loss correction factor has shown a higher error in power prediction than the experimental data. The results have shown that the power and thrust are susceptible to the smearing factor and time step size; however, the wakes of the turbines are not much affected. Therefore, the wakes can be captured by the coarser grid resolutions. However, the tip loss correction should be applied for improved power estimation. The study did not present the effect of the coarser grid on the axial and tangential loading of the turbine blades.

Sorenson et al. [27] performed the LES simulation on the NTNU model wind turbine to analyze the details of the wake behind the wind turbine in the atmospheric turbulence. The PISO algorithm was applied, and the simulation results were validated against the experimental data. The turbine's blade was divided into 43 actuator force elements with mesh composed of a very fine resolution of 24.5 million cells. The results showed good agreement with the power and thrust coefficients with a maximum error of just 9% compared to the experimental results. The study also derived the expression to estimate the near wake length.

The ALM code implementation in OpenFOAM to simulate the vertical axis wind turbine is done by Bachant et al. [28]. The ALM code includes dynamic stall, tip correction, added mass, and flow

curvature correction to study the near wake dynamics. The ALM code is coupled with $k-\epsilon$ RANS model and Smagorinsky LES model for low and high solidity turbine simulations, respectively. Both models overpredicted the C_p value at the large tip speed ratios. In addition, the LES simulations performed better in predicting the mean velocity profile at the turbine center plane than the RANS simulations. However, both models could not predict the turbulent kinetic energy profiles. In conclusion, the critical finding of the paper is that the ALM simulations can perform better than the ADM or potential flow-based vortex models.

1.2 Multirotor System

In recent years, the wind power industry has shifted its focus toward offshore wind turbines due to the better wind conditions offshore. The wind turbine sizes (blade length) have also increased in the past few decades. As a result, the blade's manufacturing costs have increased, and the transportation, installation, operation, and maintenance of large offshore wind farms become more expensive as the blade size becomes hard to handle. These concerns introduced the new concept of a multi-rotor system that consists of smaller components and can be handled by smaller machinery, reducing the levelized cost of energy (LCOE). Therefore, the Vestas has developed and performed experiments on the multi-rotor system [29].

To measure the aerodynamic performance of the multi-rotor system compared to the single rotor system, researchers have done CFD simulations of the multi-rotor system using the actuator disk modeling [14, 30]. However, for analyzing the multi-rotor system, it is desirable to have knowledge of the blade details, tip vortices, and the boundary layer on the blades because these effects will be visible on the blades of the adjacent rotors when the blade of the turbines pass each other. Unfortunately, this actuator disk modeling lacks these features. However, the actuator line method fulfills the mentioned criteria and can better predict power, blade loading, and near wake structures than the actuator disk theory. Therefore, ALM simulations of a multi-rotor will be conducted to measure the aerodynamic performance of the multi-rotor system in comparison to the single rotor.

1.3 Objectives

The studies on the ALM in CFD for wind turbine simulations have shown ambiguity in determining the ALM parameters such as projection radius, grid resolution, velocity sampling, and temporal size selection. Therefore, the objectives of this thesis are as follows:

1. Study the background theory on the wind turbine simulations.
2. Simulate the NTNU model wind turbine and MEXICO rotor using the actuator line model in the OpenFOAM software.
3. As inspired by the work of Jha et al. [21] for ALM-LES type simulations of wind turbines, this thesis implements the elliptic Gaussian radius method on the turbinesFOAM library in OpenFOAM. It then compares the elliptic Gaussian radius method against the constant grid and chord-based Gaussian radius method on the NTNU model wind turbine and MEXICO rotor.
4. Extract and compare the power, thrust, and spanwise blade loading results with the experimental results.
5. Simulate the multi-rotors (two-rotors) side by side based on the evaluated ALM parameters and perform the grid study.
6. Extract the results of power, thrust, spanwise blade loadings, and the wake structure of the multirotor turbine and compare them with the single rotor turbine.

1.4 Scope

The scope of the work is smoothing the ALM-LES simulation for the HAWT. The main focus of the thesis is improving the actuator force projection radius along the blade span because the rotor power and blade tip loading are susceptible to this ALM parameter. Due to the recent industry trend toward the multi-rotor wind turbines, the second part of the thesis covers the ALM simulation of the multi-rotor wind turbines. Therefore, the second part focuses on the aerodynamic performance of a multirotor wind turbine compared to a single rotor wind turbine. The study is composed of six chapters:

1. The first chapter covers the introduction, literature review, and purpose of the study.

2. The second chapter gives an overview of the theories on wind turbine analysis.
3. The governing equation and methodology proposed for smoothing the ALM simulation and the type of wind turbine chosen for the analysis are discussed in the third chapter
4. The details of the domain, grid sizes, and solvers chosen for study are presented in the fourth chapter.
5. The fifth chapter contains the results and discussion. The first part covers the effects of methods chosen for smoothing the ALM parameter on wind turbine blade loading, power, and thrust. The second part discusses the results of the multi-rotor wind turbine.
6. Finally, the conclusion and suggestions for future work based on the results obtained are presented in the sixth chapter.

CHAPTER 2 THEORY

There have been several theories on the research of wind energy. The first theory for understanding was the one-dimensional momentum theory. As the study progressed, Glauert [10] developed the generalized momentum theory that incorporated the rotation of the disk and the blade element momentum theory that included the blade geometry, number of blades, and airfoil properties. Nevertheless, the one-dimensional momentum theory can give a basic understanding of wind turbines.

2.1 One-dimensional Momentum Theory

The one-dimensional momentum theory, also known as actuator disk theory, is the simplest way to understand the basics of power extraction from the wind turbine. The theory idealizes the fluid as 1D, inviscid, incompressible, and irrotational. In this theory, the wind turbine rotor act as a disk without considering its geometrical attributes. The flow is contained in the imaginary stream tube where the disk is placed. Since the disk represents the rotor, it extracts the energy from the flow that reduces the velocity of air downstream, resulting in the expansion of the stream tube shown in Figure 2-1.

The thrust and power contained in the area are given as:

$$P_{air} = \frac{1}{2}\rho U_{\infty}^{3} A \tag{2.1}$$

$$T_{air} = \frac{1}{2}\rho U_{\infty}^{2} A \tag{2.2}$$

The normalization of power and thrust extracted from the wind gives the thrust and power coefficient:

$$C_T = \frac{T}{T_{air}} \tag{2.3}$$

$$C_p = \frac{P}{P_{air}} \tag{2.4}$$

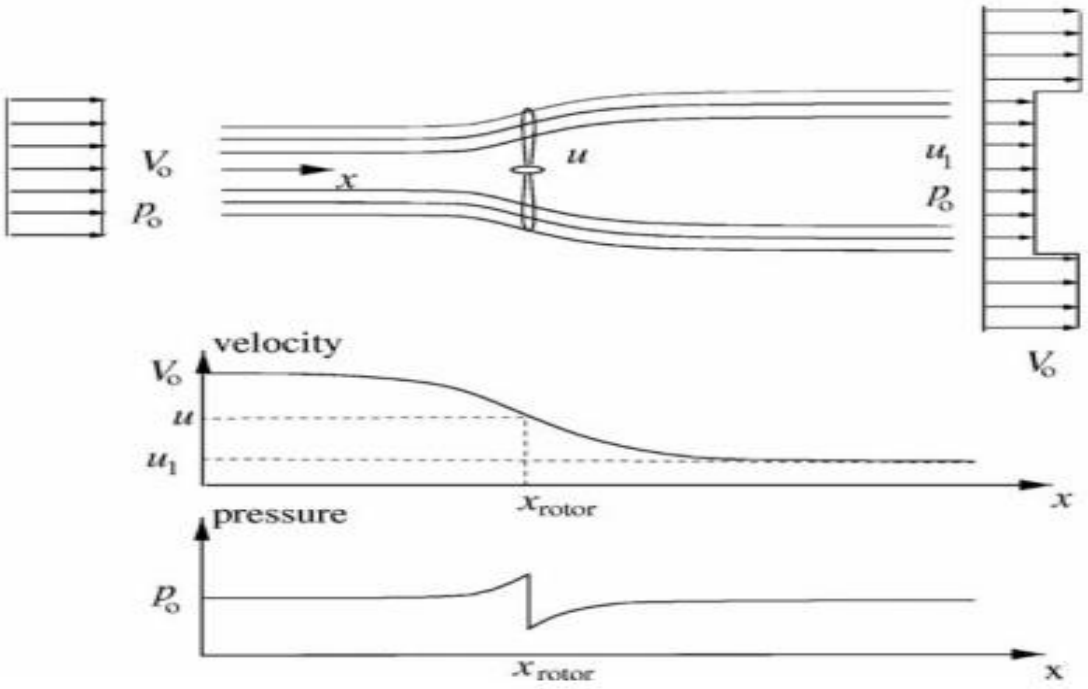

Figure 2-1 Illustration of streamline, velocity, and pressure across the rotor [31]

The pressure is assumed to be constant in near and far wake resulting in the smooth reduction of the velocity of the stream tube. The ratio of the decrease in velocity $U - U_r$ to the incoming velocity gives the axial induction factor as

$$a = 1 - \frac{U_r}{U_\infty} \tag{2.5}$$

Applying the energy conservation and momentum at a control volume (stream tube) gives the power extracted by the turbine from the wind. Then, using the Bernoulli equation, the power and thrust extracted from the wind in terms of axial induction factor are given as:

$$C_T = 4a(1 - a) \tag{2.6}$$

$$Cp = 4a(1 - a)^2 \tag{2.7}$$

Differentiation of the equation (2.7) gives the maximum amount of energy that can be extracted from the wind, known as the Betz limit.

$$\frac{dC_p}{da} = 4a(1-a)(1-3a) = 0 \tag{2.8}$$

The roots of equation (2.8) state that when the axial induction factor has a value of 1/3, it gives the C_p value of 59%, the limit of the power extracted in the idealized condition. In reality, turbines have a value less than the Betz limit.

2.2 Generalized Momentum Theory

Glauert [10] established the generalized momentum theory and improved the 1-D momentum theory in 1932 by describing the motion of a helicopter's propeller. The rotation is added to the actuator disk described in 1D momentum theory that rotates with the angular velocity ω. When the disk rotates with the angular velocity ω, it causes the wind wake to rotate in the opposite direction adding the tangential induction factor a', and as the rotor angular speed increases, wind wake rotation C_θ decreases as seen from the Figure 2-2.

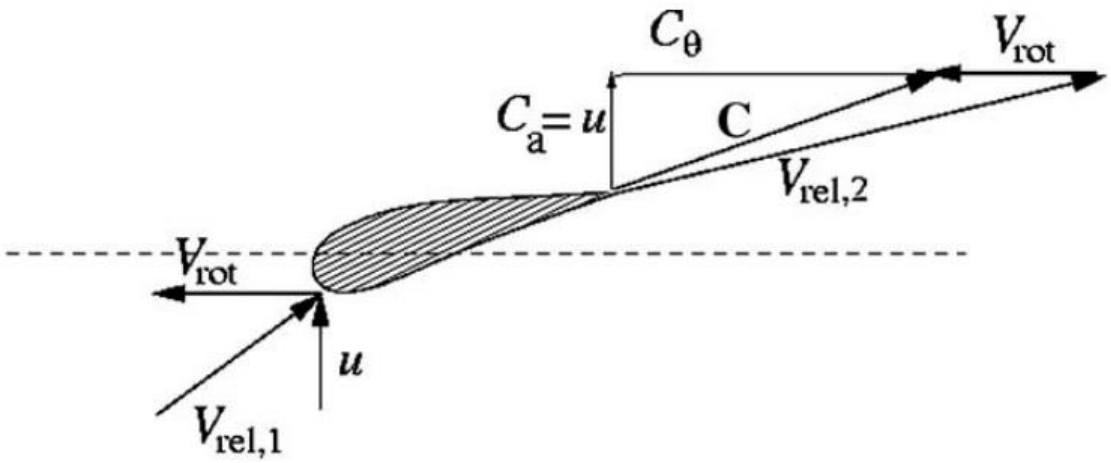

Figure 2-2 Velocity triangle for the airfoil at rotor section [31]

Hence, the important parameters are the tangential axial induction factor, tip speed ratio, and the local speed ratio given as

$$a' = \frac{C_\theta}{2r\omega} \tag{2.9}$$

$$\lambda'(r) = \frac{\omega r}{U_\infty} \tag{2.10}$$

$$\lambda = \frac{\omega R}{U_\infty} \tag{2.11}$$

The power coefficient is obtained by applying conservation of angular momentum to the flow stream and integrating it from root to tip as

$$Cp = \frac{8}{\lambda^2}\int_0^\lambda a'(1-a)\lambda^3 d\lambda \tag{2.12}$$

The above equation clear states that the maximum power coefficient can only be achieved by optimizing the factor $a'(1-a)$. Since the induced velocity is perpendicular to the relative velocity, these yields

$$\lambda'^2 a'(1+a') = a(1-a) \tag{2.13}$$

by differentiating equation (2.13) while optimizing equation (2.12) yield the optimum tangential induction factor as a function of the axial induction factor as

$$a' = \frac{1-3a}{4a-1} \tag{2.14}$$

By tabulating the value of a', a', and λ' for different rotational velocities, it is seen that as the rotational velocity ω increases, the local tip speed ratio increases to achieve optimum value when $a = 1/3$. It can be seen from Figure 2-3 that when the tip speed ratio approaches infinity, it extracts the maximum power equal to the Betz limit.

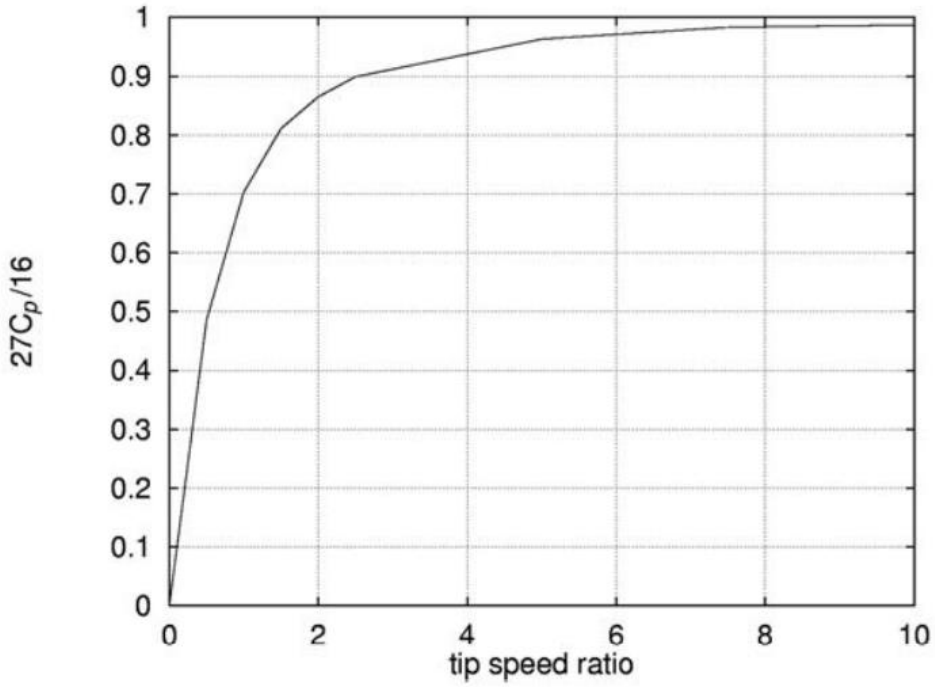

Figure 2-3 Optimum turbine efficiency versus tip speed ratio [31]

2.3 Blade Element Momentum Theory

Glauert [10] introduced the BEM approach in 1935, a simple method for modeling the rotor, which is still extensively used today. Unlike the 1D momentum theory, where twist and chord distribution of airfoil are not considered, this model can incorporate these parameters to calculate steady loads, power, and thrust for various wind speeds, pitch and twist angles, and rotational speeds. It couples the momentum theory locally on the actual blades as the stream tube in section 2.1 is discretized into the N annular elements of length dr shown in Figure 2-4.

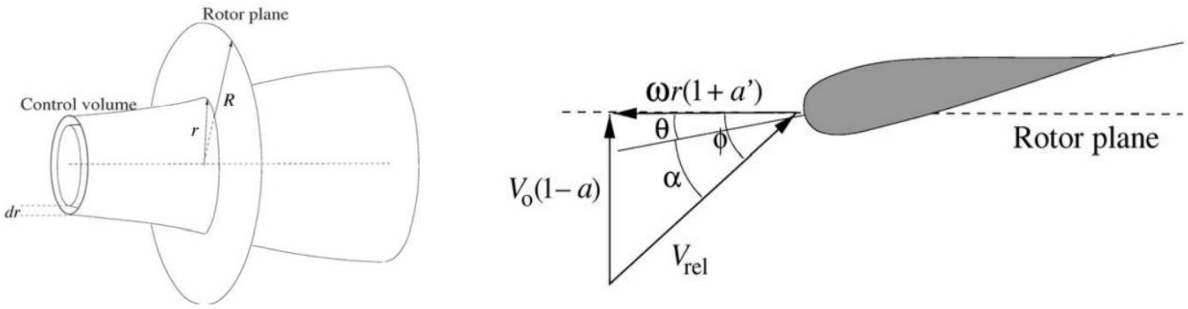

Figure 2-4 (left) Annular cross-section of stream tube, (right) velocity at rotor plane [31]

The thrust and torque for the annular section are given as:

$$dT = 4\pi r\rho U_\infty a(1-a)dr \tag{2.15}$$

$$dM = 4\pi r^3\rho U_\infty a'(1-a)dr \tag{2.16}$$

The lift and drag force per unit length can be calculated as:

$$F_d' = \frac{1}{2}\rho C_d U_{rel}^2 c \tag{2.17}$$

$$F_l' = \frac{1}{2}\rho C_l U_{rel}^2 c \tag{2.18}$$

The normal forces and tangential forces at a rotor plane are given in terms of flow angle:

$$F_n' = F_d' \sin\phi + F_l' \cos\phi \tag{2.19}$$

$$F_t' = F_d' \cos\phi + F_l' \sin\phi \tag{2.20}$$

The lift and drag coefficients are given as

$$C_n = \frac{F_n'}{\frac{1}{2}\rho V_{rel}^2 c} = C_l \cos\phi + C_d \sin\phi \tag{2.21}$$

$$C_t = \frac{F_t'}{\frac{1}{2}\rho V_{rel}^2 c} = C_l \sin\phi + C_d \cos\phi \tag{2.22}$$

The differential thrust and torque can be calculated using equations (2.21) and (2.22) as

$$dT = BF_n' dr = \frac{1}{2}\rho B \frac{U_\infty^2 (1-a)^2}{\sin\phi} c C_n dr \tag{2.23}$$

$$dM = \frac{1}{2}\rho B \frac{\omega r U_\infty (1-a)(1+a')}{\sin\phi \cos\phi} c C_t r dr \tag{2.24}$$

The values of axial induction factor a and tangential induction factor a' are as follows:

$$a = \frac{1}{\frac{4\sin^2\phi}{\sigma C_n} + 1} \tag{2.25}$$

$$a' = \frac{1}{\frac{4\sin\phi\cos\phi}{\sigma C_t} - 1} \tag{2.26}$$

Where σ is the solidity.

As all the expressions are present, the algorithm of the BEM method can be applied as follows:

1. Guessing a and a'.
2. Calculating the flow angle ϕ.
3. Calculating the angle of attack.
4. Finding lift and drag coefficient from airfoil table.
5. Calculating the C_n and C_t.
6. Calculating the a and a'.
7. Repeating step 2 until a and a'converges
8. Calculating the local loads on the blade segments.

This algorithm represents the blade element method. However, for the excellent result, it is necessary to apply the two tip corrections, namely, Prandtl's tip loss factor, which rectifies the infinite number of blade assumptions, and Glauret correction, which creates an empirical relation between the thrust coefficient C_T and axial induction factor a.

2.3.1 Prandtl's Tip Loss Factor

Prandtl's tip loss factor assumes a finite length of blades instead of an infinite length of blades. As a result, the vortex system in the wake region contrasts with that of the infinite number of blades. The factor P_f is added to the thrust and torque equations.

$$P_f = \frac{2}{\pi}\cos^{-1} e^{\frac{B\,(R-r)}{2r\sin\phi}} \tag{2.27}$$

This yields axial and tangential induction factors as:

$$a' = \frac{1}{\frac{4P_f \sin\phi\cos\phi}{\sigma C_t} - 1} \tag{2.28}$$

$$a = \frac{1}{\frac{4P_f\, sin^2\phi}{\sigma C_n} + 1} \tag{2.29}$$

In the algorithm, extra step 2 is added for the Prandtl's factor calculation, and in step 6, axial induction factor a and tangential induction factor a' are calculated from equations (2.28) and (2.29).

2.3.2 Glauert Correction

For the axial induction factor $a > 0.4$, the momentum theory fails. Hence, Glauert [10] corrected the thrust coefficient empirically by fitting the curve to the measured data shown in Figure 2-5. The correction coefficient as a function of spanwise location is added to the blade elements.

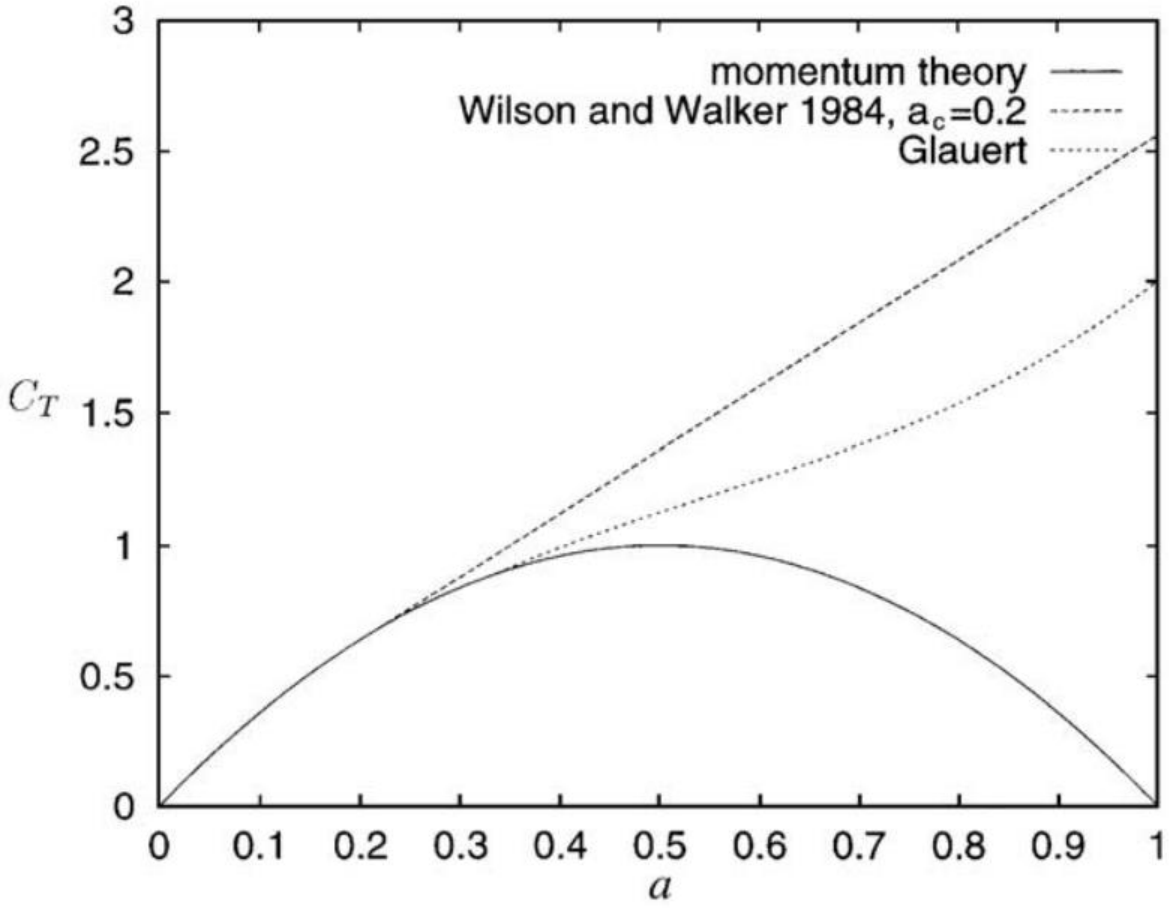

Figure 2-5 Glauert corrected curves of C_T versus axial induction factor a [31]

2.4 Actuator Line Method in CFD

The solution domain consists of the solid entities in the conventional CFD simulation. The boundary conditions on the surface are applied, such as no-slip and wall function, to introduce turbulence in the solution. However, using this method requires a large number of cells in the mesh to fully resolve the boundary layer that comes at a very high expense of computational cost. Furthermore, to add to the difficulty, rotation of the wind turbine blades makes simulation highly unsteady, requiring approaches such as Sliding Mesh Interface (SMI) or Multireference Frame (MRF). In SMI, the mesh physically moves in different regions and the mesh boundaries moving against each other require special treatment. On the other hand, the whole domain is geometrically stationary, and the moving zones are modeled by adding the term in the conservation equations in

the MRF approach. Therefore, developing the numerical model was necessary to account for these drawbacks.

Figure 2-6 The discretization of the blades into the lines with each section representing the force [32]

Sorensen and Shen [15] introduced the actuator line method for CFD simulation of wind turbine rotors. The model combines the blade element theory with the Navier-Stokes equation. In this approach, unlike the blade element method, where the physical geometry of the blade is divided into sections, the line representing the blade is divided into sections, as shown in Figure 2-6. Each section of the line describes the actuator point, which has geometrical properties, i.e., chord, twist, radial position, and airfoil lift and drag data. The 2D airfoil theory calculates the aerodynamic forces on these actuator points. The angle of attack and velocity magnitudes are also needed for the calculations, whose values are extracted from the solution domain. The process of extracting the data from the solution domain is known as velocity sampling, and the actuator force calculation is susceptible to this parameter. The C_l and C_d data are avaihlable in the ALM method, requiring no computation during runtime, reducing the computational cost. The Reynolds number varies along the blade because of the variable chord length. Therefore, the calculated force must be smeared among the cells around the actuator point rather than applying it on the closest cell as a

single force. This force smearing is done in the form of a sphere shape through 3D Gaussian distribution.

$$\eta_{N,i} = \frac{1}{\varepsilon^2 \pi^{\frac{3}{2}}} \exp\left[-\left(\frac{|\boldsymbol{r}|}{\varepsilon}\right)^2\right] \tag{2.30}$$

The ε parameter in this distribution equation controls the smearing forces, and the solution obtained is sensitive to this parameter. The poor value of ε can cause oscillation in the system. The simulations are also highly sensitive to time step size and grid resolutions.

CHAPTER 3 METHODOLOGY

This study performs the CFD simulations of the NTNU model wind turbine and MEXICO rotor using the actuator line model in OpenFOAM. The obtained results for the NTNU wind model are compared and validated with the wind tunnel experiment [33]. Similarly, the MEXICO rotor simulation results are compared with the results of the New Mexico experiment in the Mexnext-III report [34]. Bachant et al. [35] developed the turbinesFOAM library extension in OpenFOAM to model the turbines using the ALM method. The ALM method introduces the turbine into the Navier-Stokes equation as a body force. The blade element data of the NTNU turbine is obtained from the blind test report by Krogstad et al. [36], while for the Mexico rotor, it is extracted from the Mexnext-III project website. After simulating and verifying the results of a single MEXICO rotor, the multi-rotor systems are simulated using two MEXICO rotors. The power output, blade loading, and wakes results of the multi-rotor are compared against the single rotor.

3.1 Governing Equations

The NTNU model wind turbine operates at the rated condition of $\lambda = 6$, while the MEXICO rotor at $\lambda = 6.7$ [33, 34]. In this study, simulations are carried out for the NTNU wind turbine and MEXICO rotor with the windspeed $U_\infty = 10\ m/s$ and $U_\infty = 15\ m/s$, which gives Mach number Ma_{tip} = 0.17 and $Ma_{tip} = 0.29$ at the tip of the blade, respectively. Therefore, with this low Mach number, the flow can be assumed incompressible. The incompressible flow can be represented by the conservation of mass and momentum as:

$$\nabla . \boldsymbol{u} = 0 \tag{3.1}$$

$$\frac{\partial}{\partial t}\boldsymbol{u} + \nabla.(\boldsymbol{uu}) = -\nabla p + +\nabla.2\nu\boldsymbol{D} + \boldsymbol{S} \tag{3.2}$$

Where $\boldsymbol{u}$ is the velocity, $\boldsymbol{D}$ is the strain rate tensor, and **S** is the source term.

In the tensorial form

$$\frac{\partial u_i}{\partial x_i} = 0 \tag{3.3}$$

$$\frac{\partial u_i}{\partial t_i} + \frac{\partial}{\partial x_j}(u_j u_i) = -\frac{\partial p}{\partial x_i} + \frac{\partial}{\partial x_j}\left(2\nu \mathrm{D}_{ij}\right) + S_i \tag{3.4}$$

Where strain rate tensor D_{ij} is given as

$$\mathrm{D}_{ij} = \frac{1}{2}\left(\frac{\partial u_i}{\partial x_j} + \frac{\partial u_j}{\partial x_i}\right) \tag{3.5}$$

The source term S_i is important here, as it represents the body force vector that is blade forces calculated from the ALM method and is passed into the solution domain (See sec 3.1.2). By use of the continuity equation, equation (3.2) can be rewritten to give the incompressible Navier-Stoke equation as:

$$\frac{\partial}{\partial t}\boldsymbol{u} + \boldsymbol{u}.\nabla\boldsymbol{u} = -\nabla p + v\nabla^2\boldsymbol{u} + \boldsymbol{S} \tag{3.6}$$

In CFD, this equation can be solved using the direct numerical simulation (DNS) to calculate all the turbulences accurately but at the high expense of computational cost, even at a very low Reynolds number. However, due to this reason, two standard turbulence modeling techniques are used in CFD, namely RANS and LES. In this study, large-eddy simulations will be used.

3.1.1 Large Eddy Simulation

In the large-eddy simulation, the spatial filtering operation is applied to the unsteady Navier-Stokes equation that separates the large eddies (anisotropic) from the smaller eddies (isotropic). The OpenFOAM uses the implicit filter method. The filtered equations are defined as:

$$\nabla.\overline{\boldsymbol{u}} = 0 \tag{3.7}$$

$$\frac{\partial}{\partial t}\overline{\boldsymbol{u}} + \overline{\boldsymbol{u}\nabla\boldsymbol{u}} = -\nabla p + v\nabla^2\overline{\boldsymbol{u}} + \overline{\boldsymbol{S}} \tag{3.8}$$

The bar indicates the filtered quantity. The source term $\overline{\boldsymbol{S}}$ is the body forces that are calculated in the actuator line method. As OpenFOAM uses the finite volume implementation, the filter width is defined as the average of the grid volume. The large eddies are greater than the filter width, while the small eddies that are smaller than the filter width and require modeling. The small eddies are calculated by the sub-grid scale (SGS) modeling.

3.1.1.1 Smagorinsky Model

The most widely used sub-grid scale model that was developed in the 1960s is the Smagorinsky model [37]. The model is based on the eddy viscosity assumption, which postulates a linear relationship between the SGS shear stress and the resolved rate of the strain tensor. The SGS tensor τ_{ij} is

$$\tau_{ij} = u_i u_j - u_i u_j \tag{3.9}$$

$$= \frac{1}{3}\tau_{kk} + \left(\tau_{ij} - \frac{1}{3}\tau_{kk}\delta_{ij}\right) \tag{3.10}$$

$$\approx \frac{1}{3}\tau_{kk}\delta_{ij} - 2v_{sgs}dev\overline{(D)}_{ij} \tag{3.11}$$

$$= \frac{2}{3}k_{sgs}\delta_{ij} - 2v_{sgs}dev\overline{(D)}_{ij} \tag{3.12}$$

where v_{sgs} represents the sub-grid scale eddy viscosity and $\overline{(D)}_{ij}$ is resolved-scale strain rate tensor defined as

$$\overline{(D)}_{ij} = \frac{1}{2}\left(\frac{\partial \bar{u}_i}{\partial x_j} + \frac{\partial \bar{u}_j}{\partial x_i}\right) \tag{3.13}$$

The subgrid-scale kinetic energy k_{sgs} is defined as

$$k_{sgs} = \frac{1}{2}\tau_{kk} = \frac{1}{2}(\overline{u_k u_k} - \bar{u}_k\,\bar{u}_k) \tag{3.14}$$

Sub-grid scale tensor τ_{ij} is split into two parts $\frac{1}{3}\tau_{kk}\delta_{ij}$ isotropic, and $\tau_{ij} - \frac{1}{3}\tau_{kk}\delta_{ij}$ anisotropic.

$$\tau_{ij} - \frac{1}{3}\tau_{kk}\delta_{ij} \approx 2v_{sgs}dev\overline{(D)}_{ij} \tag{3.15}$$

The sub-grid scale viscosity in OpenFOAM is given as

$$v_{sgs} = C_k \Delta_{grid} \sqrt{k_{sgs}} \tag{3.16}$$

C_k is the model constant whose default value is 0.094. The Δ_{grid} is the grid size that defines the sub-grid length scale. In the present case, $\Delta_{grid} = \sqrt[3]{dxdydz}$ is equal to the cube root of the volume of the cell.

In OpenFOAM, the assumption is to balance the subgrid-scale energy production with dissipation.

$$\overline{D} : \tau_{ij} + C_\epsilon \frac{{k_{sgs}}^{1.5}}{\Delta_{grid}} = 0 \tag{3.17}$$

The operator ':' is the double inner product of two second-rank tensors. The solution of this equation gives

$$A{k_{sgs}}^2 + Bk_{sgs} + C = 0 \tag{3.18}$$

$$A = \frac{C_\epsilon}{\Delta_{grid}} \tag{3.19}$$

$$= 2C_k \Delta_{grid} \left(dev(\overline{D}) : \overline{D}\right) \tag{3.20}$$

Where $|\overline{D}| = \sqrt{2\overline{D} : \overline{D}}$ Substituting it in the equation (3.20). This gives

$$v_{sgs} = C_k \sqrt{\frac{C_k}{C_\epsilon}} \Delta_{grid}^2 |\overline{D}| \tag{3.21}$$

In the original Smagorinsky model, this expression is given as

$$v_{sgs} = C_s \Delta_{grid}^2 |\overline{D}| \tag{3.22}$$

Where C_s is the Smagorinsky constant. Therefore, OpenFOAM implementation relates the Smagorinsky constant with the model constants as

$$C_s{}^2 = C_k \sqrt{\frac{C_k}{C_\epsilon}} \tag{3.23}$$

In OpenFOAM, the default value of C_k and C_ϵ is 1.048 and 0.094, respectively. This result in $C_s = 0.168$, which is the optimal value for isotropic turbulence.

3.1.2 Actuator Force

In equation (2.2), the source terms present are the body forces of blades introduced into the solution domain, which will be discussed in this section. In the actuator line model, the turbine blades are modeled as a virtual line incorporated into the blade element theory (BEM), dividing the line into a finite number of sections. The section represents the actuator point in the domain. The force is calculated at each actuator point and moved in the momentum equations as a body force. As a result, the turbine representation is independent of physical surface and boundary conditions. The drag and the lift forces are computed at these actuator points given as:

$$F_d = \frac{1}{2}\rho C_d U_{rel}^2 A \tag{3.24}$$

$$F_l = \frac{1}{2}\rho C_l U_{rel}^2 A \tag{3.25}$$

Where C_d and C_l are the drag and lift coefficient, respectively. Their values are obtained from the known tabular data at the various angle of attacks at a specified Reynolds number and are linearly interpolated. In addition, A_s is the section area and U_{rel} is free stream velocity. These forces are then transformed into the rotor coordinate system. After the calculation, the forces are introduced as a source term in the momentum equation. Therefore, the equation (3.2) becomes:

$$\frac{\partial}{\partial t}\boldsymbol{u} + \boldsymbol{u}.\nabla\boldsymbol{u} = -\nabla p + v\nabla^2\boldsymbol{u} + \boldsymbol{f_b} \tag{3.26}$$

In the SGS model, after filtering:

$$\frac{\partial}{\partial t}\bar{\boldsymbol{u}} + \overline{\boldsymbol{u}\nabla\boldsymbol{u}} = -\nabla p + v\nabla^2\bar{\boldsymbol{u}} + \overline{\boldsymbol{f_b}} \tag{3.27}$$

Where $\boldsymbol{f_b}$ is the body force representing along the actuator line.

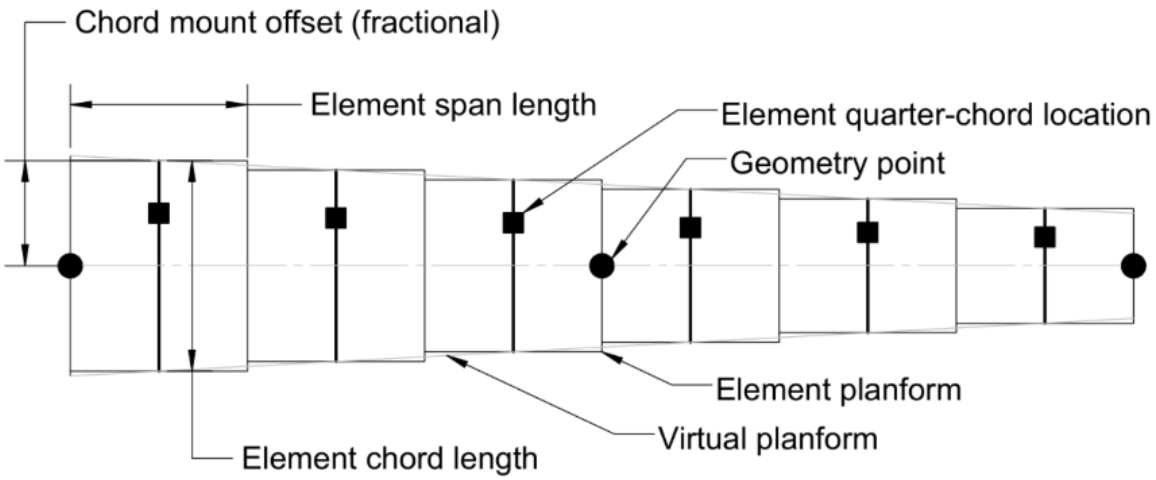

Figure 3-1 Actuator line discretization into actuator line elements [38]

In ALM, the force and velocities fields are highly coupled, and results are susceptible to these criteria. The velocity sampling for each actuator point is done at the quarter chord position in the turbineFoam library using OpenFOAM's interpolationCellPoint class, as seen in Figure 3-1. The force vector $\boldsymbol{f_{N,i}}$ calculated at each actuator point cannot be directly passed into the solution domain as it will cause singularity or oscillation in the solution. Instead, this issue is handled by *smearing* the calculated forces at each vicinity of the actuator point. The widely used approach is the Gaussian distribution, in which the Gaussian kernel function $\eta_{N,i}$ is given as

$$\boldsymbol{f_b}(x_p, y_p, z_p, t) = \sum_N \sum_i \boldsymbol{f_{N,i}}(x_{N,i}, y_{N,i}, y_{N,i})\eta_{N,i} \tag{3.28}$$

$$\eta_{N,i} = \frac{1}{\varepsilon^2\pi^{\frac{3}{2}}}\exp\left[-\left(\frac{|\boldsymbol{r}|}{\varepsilon}\right)^2\right] \tag{3.29}$$

Where $\boldsymbol{r}$ is the distance between the grid point to the actuator element $N_{n,i}$. ε is the parameter that is called the Gaussian radius. The Gaussian radius ε controls the force smearing, which has been

a discussion subject in the ALM. In this case, the ALM simulation of the model turbine will be performed based on the Gaussian radius ε parameter studied in previous literature. Therefore, the three methodologies for defining the Gaussian radius ε that will be studied here are:

1. Gaussian radius ε is twice the size of the local grid spacing Δ_{grid} , according to Troldborg [19].
2. Gaussian radius ε as a function of the chord length [24, 20].
3. Finally, Gaussian radius ε is defined as the equivalent elliptic planform, according to Jha et al. [21].

3.1.3 Equivalent Elliptic Planform Method and Grid Resolution Criteria.

Instead of using the average chord base criterion, Jha et al. [21] proposed the hypothesis that the choice of Gaussian radius ε should be based on the elliptic planform of the same aspect ratio as the actual blade. The detail of the proposed method for finding the ALM parameters ε, Δ and, Δ_p are described in the original paper [21]. The summary of which is as follows:

1. Finding the blade aspect ratio

$$AR = \frac{R}{\bar{c}} \tag{3.30}$$

$$\bar{c} = \frac{1}{R}\int_0^R c(r)dr \tag{3.31}$$

Where R is the radius and $\bar{c}$ is the average chord length.

2. Determining elliptic planform with the same AR

$$c^*(r) = c_o\sqrt{1-\left(\frac{2r}{R}\right)^2} \tag{3.32}$$

$$c_o = \frac{4}{\pi}\bar{c} \tag{3.33}$$

3. Discretization of the equivalent ellipse for $\Delta_{grid}/R \leq 1/30$. The minimum discretization level is:

$$\varepsilon_{R/2} = n_{min}\Delta_{\text{grid}} \tag{3.34}$$

The $n_{min} = 1$ gives the minimum discretization threshold on any grid as:

The work of Jha et al. shows that instabilities occur when $n_{min} = 0$ [32].

$$\varepsilon_o = n_{max}\Delta_{\text{grid}} \tag{3.35}$$

Where the value of n_{max} is determined from

$$\frac{n_{max}\Delta_{grid}}{R} \approx 0.08 \ldots 0.10 \tag{3.36}$$

By following the $\Delta_{grid}/R \leq 1/30$, it states $n_{max} \geq 3$. One of the aim of this study is to verify the value of n_{max}. By combining the equations (2.30), (2.32), 2.35), and(2.36), it states

$$\frac{\varepsilon}{c^*} = \frac{\varepsilon_o}{c_o} = 0.25\left(\frac{n_{max}\Delta}{\text{R}}\right)(\pi AR) \tag{3.37}$$

It should satisfy the minimum threshold criteria such that

$$\varepsilon(r) = MAX\big(\varepsilon(r), \varepsilon_{R/2}\big) \tag{3.38}$$

4. Actuator spacing should satisfy the criteria of

$$\frac{\Delta_b}{\Delta_{grid}} \geq 1.5 \tag{3.39}$$

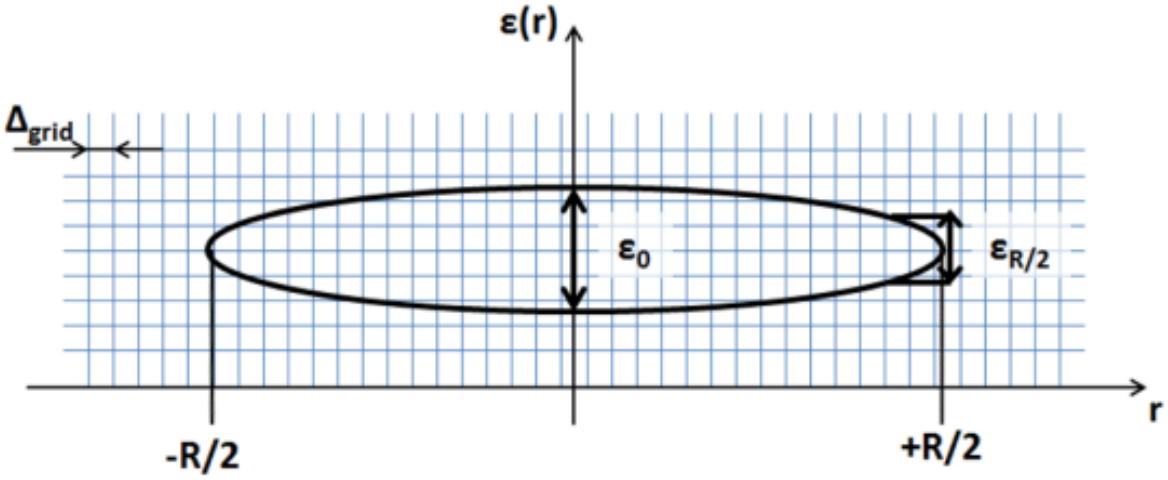

Figure 3-2 Equivalent elliptic distribution for the Gaussian radius ε. This Gaussian radius varies from $-R/2$ to $R/2$ and is represented just for demonstration purposes. In actuality, the equivalent elliptic planform was shifted such that $0 \leq r \leq +R$ [21]

Since the actuator line consists of the discretized segments and the actuator point lies in the middle of these segments, none of the actuator points is consistent with the tip and root of the blade. Equation (3.39) and equation (3.34) confirm that when the Gaussian radius projects the actuator point force at a point next to the blade tip and the root, the projected force at the actual tip and root is only 10% of its peak value adjacent to the actuator points. Thus, the three-dimensional Gaussian does not smear the body forces outside the blade tip and root. Furthermore, the equivalent elliptic planform c^* is only used to define the Gaussian radius ε along the blade span, while the actual blade chord distribution c is used to calculate blade forces. Jha et al. proposed n_{max} value of 3 and 6 for the coarse grid of $\Delta_{grid}/R = 1/30$ and the fine grid of $\Delta_{grid}/R = 1/60$, respectively, for the NREL phase VI rotor and NREL 5 MW turbine [21]. In addition, the work suggested that the equation (3.36) just provides the guidelines for choosing the n_{max} value and is not a rule of thumb. Therefore, this work aims to simulate the different wind turbines to verify the n_{max} values in equation (3.36), keeping in view the guidelines.

3.2 NTNU Model Turbine

The NTNU model turbine has a rotor diameter of $0.9\ m$, the hub diameter is $0.09\ m$, and the tower is composed of a section of varying diameters. The blade chord length varies along the radius consisting of different sections of the S826 airfoil. Figure 3-4 shows the distribution of twists along the length of the blade. Further information about turbine blades and airfoil characteristics is present in the Krogstad and Lund [39]. The equivalent elliptic planform for the NTNU turbine blade to define the Gaussian radius ε is shown in Figure 3-5 . This elliptical planform only represents the Gaussian radius ε while the force vector is calculated using the actual blade chord distribution.

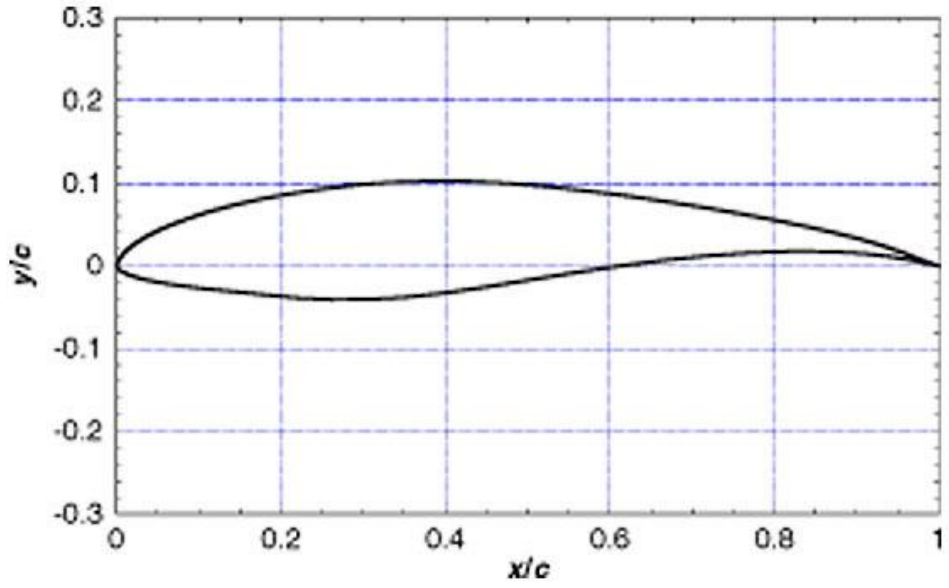

Figure 3-3 Profile of airfoil S826 [36]

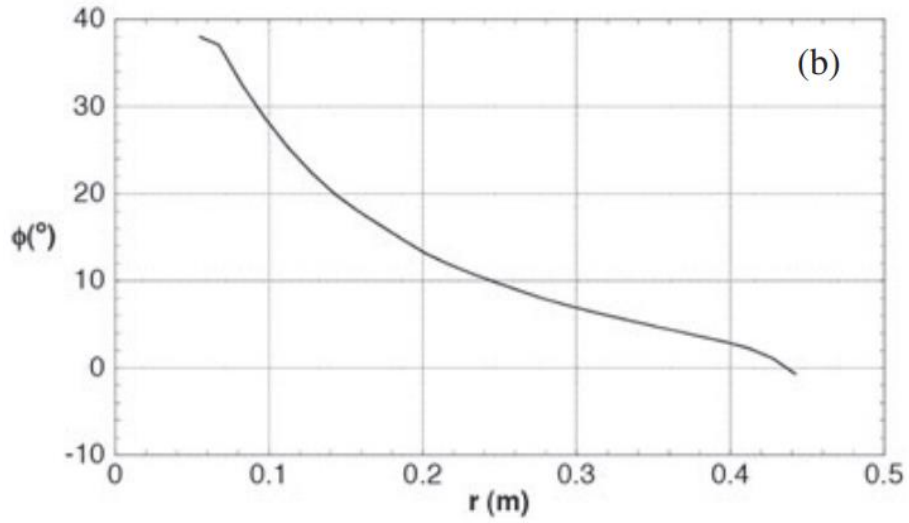

Figure 3-4 Radial distribution of twist [39]

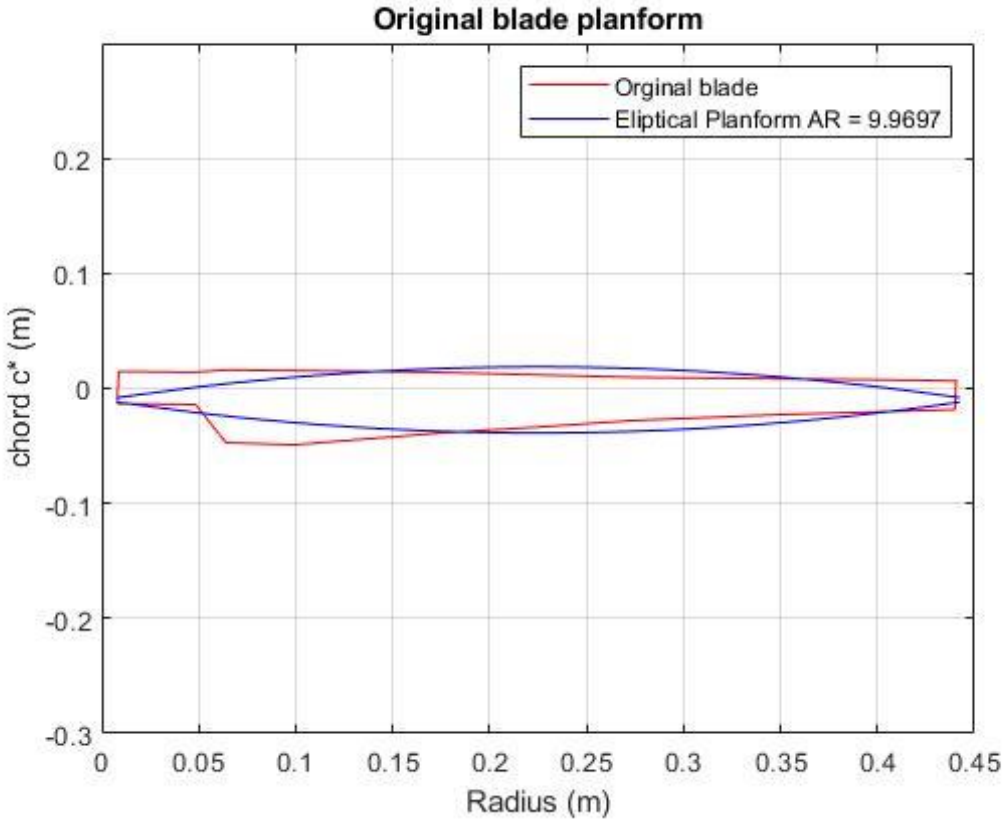

Figure 3-5 Equivalent elliptic planform of NTNU blade that defines Gaussian radius ε

3.3 MEXICO Rotor

The details of the MEXICO rotor are defined in the ECN report [34]. The MEXICO rotor is a three-bladed rotor having a diameter of $4.5\,m$. The collective pitch of the blades is $-2.3°$. The rotor has an optimal TSR value of 6.8, corresponding to the $15\,m/s$ windspeed. The rotor blades consist of three airfoils, namely, DU91-W2-250, RISØ-A1-21, and NACA 64-418. Therefore, 20 to 45.6% span length contains the DU91-W2-250 airfoil, 54.4% to 65.6% span length has the RISØ-A1-21 airfoil, and 74.4% span to tip has NACA 64-418, as seen in Figure 3-6. The equivalent elliptic planform to define the Gaussian radius ε is shown in Figure 3-8.

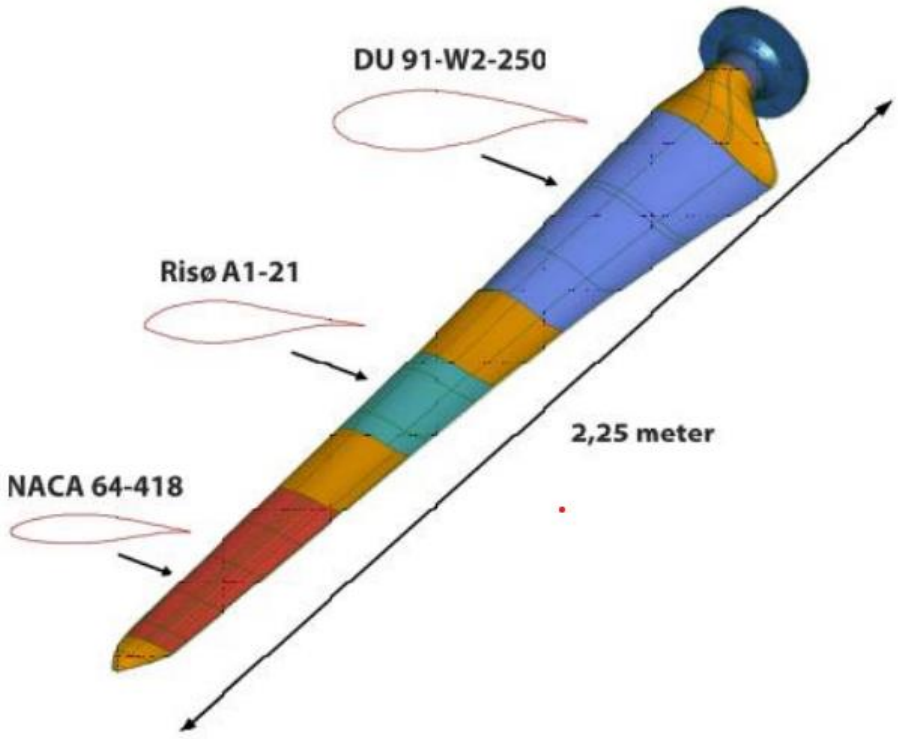

Figure 3-6 Airfoil distribution in MEXICO rotor blade [40]

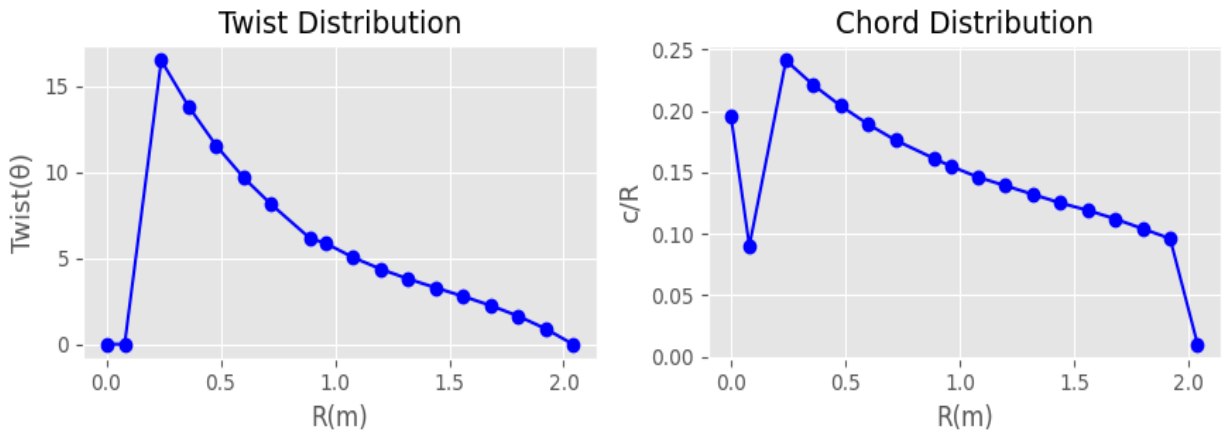

Figure 3-7 Twist (left) and chord distribution (right) along the blade of the MEXICO rotor

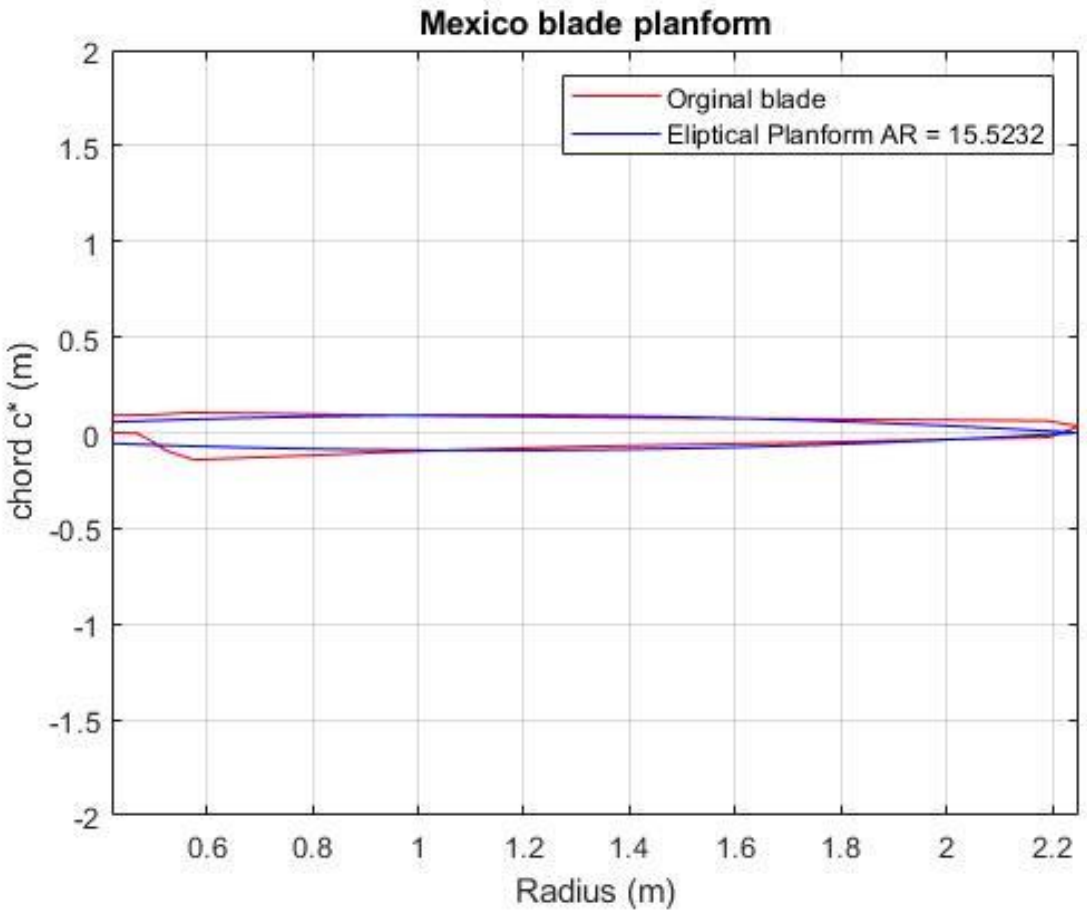

Figure 3-8 Elliptic planform for the MEXICO blade (the ellipse is cut from $0.2\ m$ root distance).

CHAPTER 4 COMPUTATIONAL SETUP

The computational setup is adjusted to replicate the wind tunnel experiment [33] for the NTNU model turbine, while the MEXICO rotor replicates the New Mexico experiments [34].

4.1 Computational Domain

The domain in this study is structured hexahedral mesh, generated using the built-in blockMesh utility in OpenFOAM. Moreover, it consists of different levels of refinement regions. The mesh is refined using the snappyHexMesh utility in OpenFOAM. Therefore, the mesh is composed of both structured and unstructured parts. However, the meshes are generated for all simulations with a unity aspect ratio.

4.1.1 Computational Domain for NTNU Model Turbine

The domain extends from $-4.5\ D$ to $+9\ D$ in the stream-wise direction and $-1.6\ D$ to $+1.6\ D$ in the lateral and longitudinal direction. The hub of the rotor is at the origin. The domain consists of the four refinement regions shown in Figure 4-1. The three-refinement level is applied in box shape form using snappyHexMesh utility, finest refinement at the rotor region $\pm 0.7\ D$ in stream-wise direction while $\pm 0.8\ D$ in the lateral (y, z) direction. The second level starts from $-2.3\ D$ upstream to $+6.6\ D$ downstream, and $1.1\ D$ in the lateral (y, z) direction. Finally, the third refinement level starts from $-2.5\ D$ to $8.8\ D$ downstream. The grid resolution at the rotor area is $\Delta_{grid}/R = 1/43$, and the number of cells for this resolution is approximately 5.4 million.

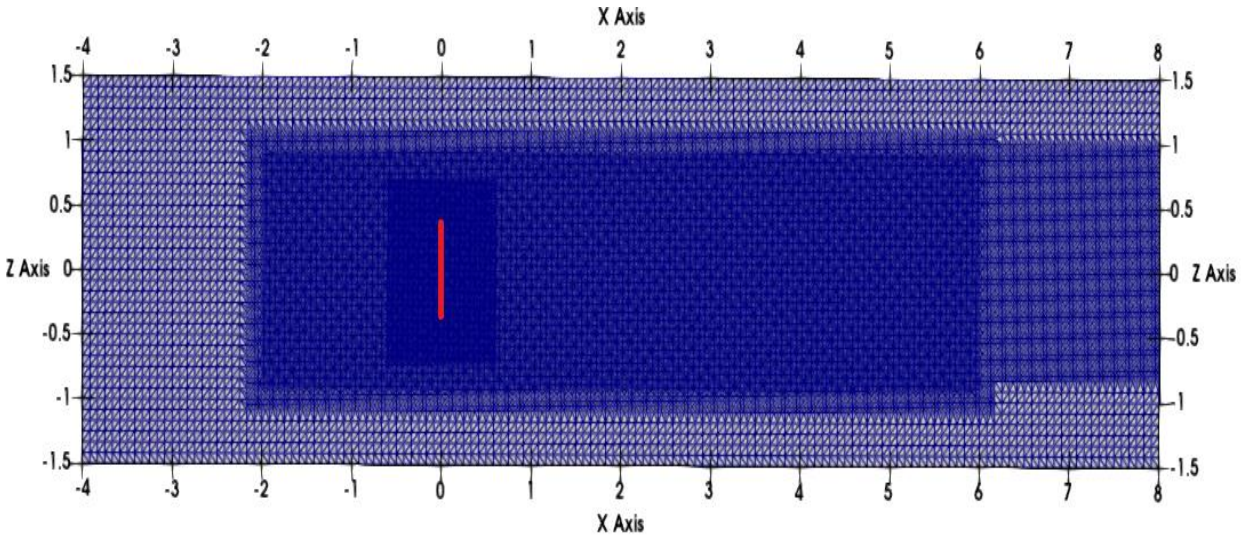

Figure 4-1 Front view domain for NTNU Model turbine $\Delta_{grid}/R = 1/43$

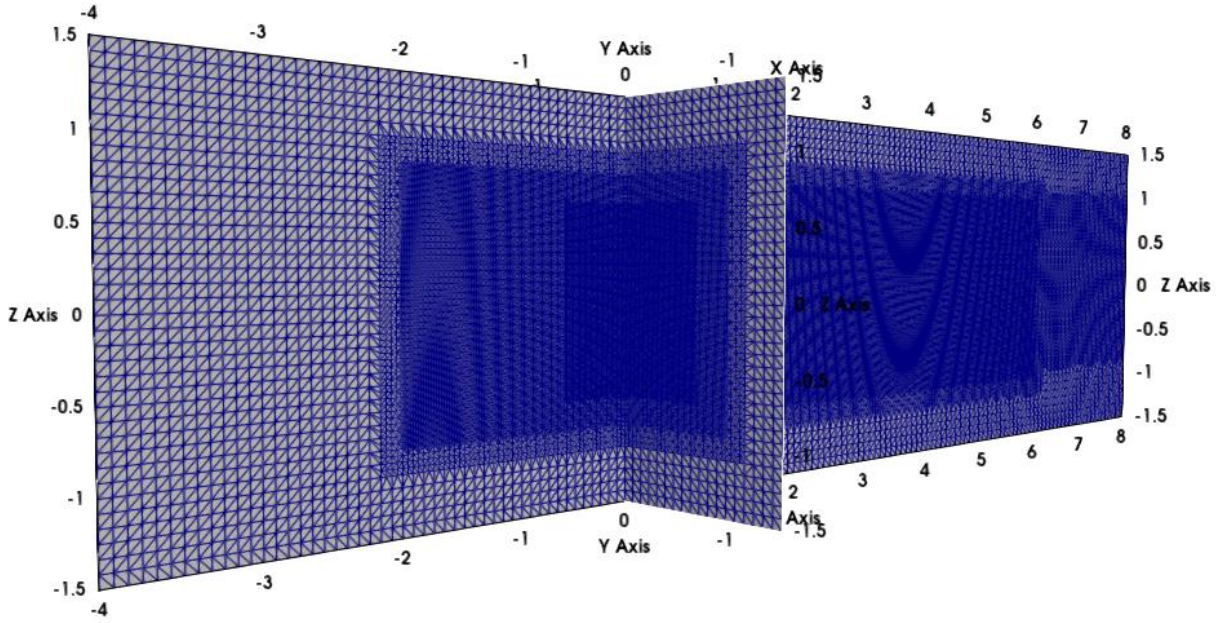

Figure 4-2 Refinement for NTNU model turbine $\Delta_{grid}/R = 1/43$ in rotor area.

4.1.2 Computational Domain for MEXICO Rotor

The size of the MEXICO domain is $40\,m$, $20\,m$, and $20\,m$ in length, width, and height, respectively, while to make the comparison between the far wake of a single rotor system with a

multi-rotor side by side, the size of the domain increased to $40\,m$, $40\,m$, and $20\,m$ in length, width, and height, respectively. The domain contains three refinement regions. For the accurate measurement of wake characteristics for single and multi-rotor systems, the finest refinement region starts from $-1.5\,D$ and extends to $+2\,D$ in a stream-wise direction, as shown in Figure 4-3. The origin is at the rotor's hub for a single rotor case, but the origin is at mid-distance between the rotors for the multi-rotor arrangement, as shown in Figure 4-4. The domain of single and multi-rotors consists of 1.1 and 2.4 million cells for grid resolution $\Delta_{grid}/R = 1/30$, respectively.

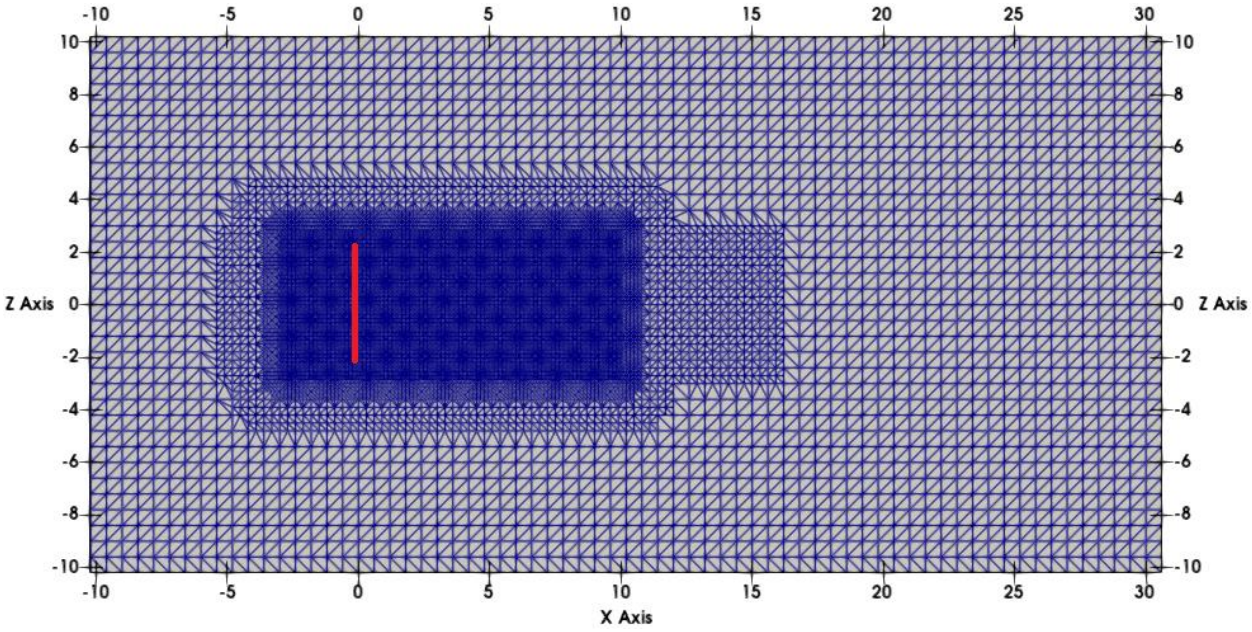

Figure 4-3 Single rotor refinement level with $\Delta_{grid}/R = 1/30$ at the rotor region, (y-plan view)

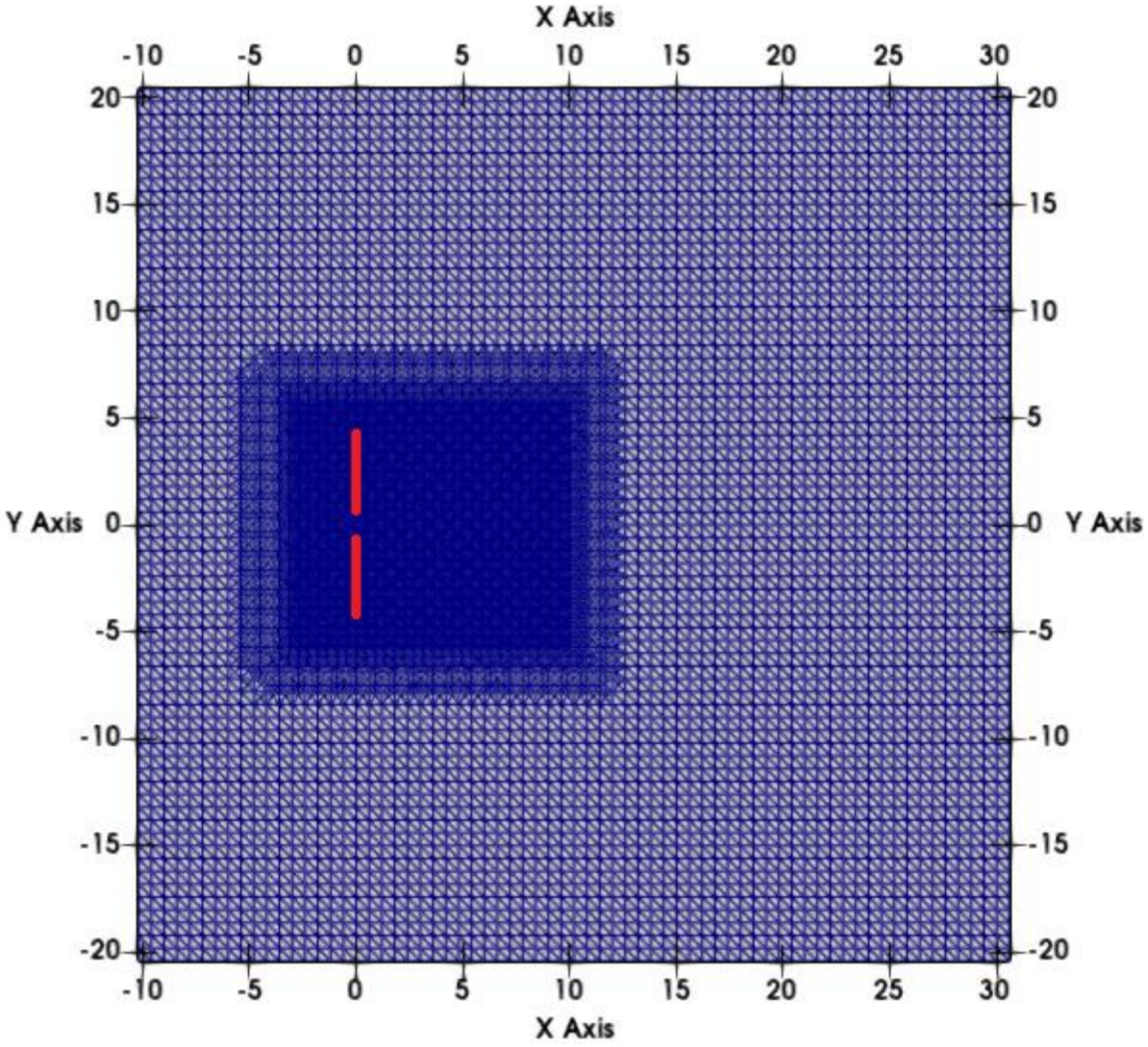

Figure 4-4 Origin is between the rotors for multi-rotor setup with $\Delta_{grid}/R = 1/30$ at the rotor region. (z-plane view)

4.2 Discretization Schemes

The same discretization schemes are used for all the simulations. The 2nd order Crank Nicholson scheme is used for the time discretization, and the 2nd order bounded upwind schemes are used for the divergence and gradient terms.

4.3 Solver

The PimpleFOAM solver is used for this simulation. The OpenFOAM transient solver for incompressible fluids to solve pressure and velocity coupling. PimpleFOAM is a hybrid combination of SIMPLE (Semi-Implicit Method for Pressured Linked Equations) and PISO (Pressure-Implicit with Splitting of Operators) algorithm. [41] The PIMPLE consists of two loops, the outer loop resembles SIMPLE iteration, and the inner loop resembles PISO iterations. In the present case, the parameter *nOuterCorrecter* is set to 1, which means the PIMPLE solver is running as a PISO solver, and the *nCorrector* is set to 2 means that pressure correction is applied twice.

4.4 Boundary Conditions

The inlet conditions are set to replicate the experiments [33, 39, 34]. The inlet velocity for the NTNU case is $10\,m/s$, while for the New Mexico case is $15\,m/s$. Table 4-1 shows the inlet conditions for the NTNU model turbine and MEXICO Rotor. The subgrid-scale turbulent viscosity is calculated as discussed in section 3.3.1.1.

Table 4-1 Boundary conditions for pressure and velocity.

	Inlet	Outlet	Top, Bottom, and sides
$\boldsymbol{U}$	Uniform (fixed)	type inletOutlet	0
$\boldsymbol{P}$	Zero Gradient	0	ZeroGradient

CHAPTER 5 RESULTS AND DISCUSSION

In this study, the ALM method is applied to the two different model wind turbines having different sizes to find the correct parameters for the wind turbine simulations that can give accurate results. The results are divided into two main sections. In the first section, the NTNU model turbine and MEXICO rotor are simulated to evaluate ALM parameters based on the previous research methods for actuator force discussed in section 3.1.2 [32, 19, 24]. While in the second section, the multi-rotor simulation is done side by side based on the previously calculated parameters, and the power, blade loading, and near wake results are compared to the single rotors.

As discussed in the previous chapters, there is no correct constant value for the simulation parameters as these methods haven't been proven appropriate for every case. Therefore, the first section investigates these ALM parameters and techniques to find the optimum values to simulate the multi-rotor system for the next section. The comparisons are made among the equivalent elliptic planform, grid-based criteria, and constant average method in defining the Gaussian radius ε parameters. The study of the projection radius, grid resolution, and temporal discretization (time step) has been done in detail. The second section includes the simulations of the multi-rotor system. The grid study analysis is also done for the multi-rotor.

5.1 ALM Parameters Study for a Single Rotor Turbine

As discussed in section 3.1.2, the actuator line parameter of the ALM method is highly sensitive. Therefore, the following parameters will be evaluated in this study:

1. Time step, Δt.
2. Grid resolution at the rotor area, Δ_{grid}/R.
3. Projection radius, ε (constant chord-based, grid base, and equivalent elliptic planform).
4. Relative actuator spacing size to the grid size, Δ_p/Δ_{grid}.

All the simulations for the MEXICO rotor are performed at the optimal $TSR = 6.7$ at the $15\ m/s$ wind speed giving the corresponding values of the tip speed $U_{tip} = 100.5\ m/s$ and rotational speed $\omega = 40.2\ rpm$.

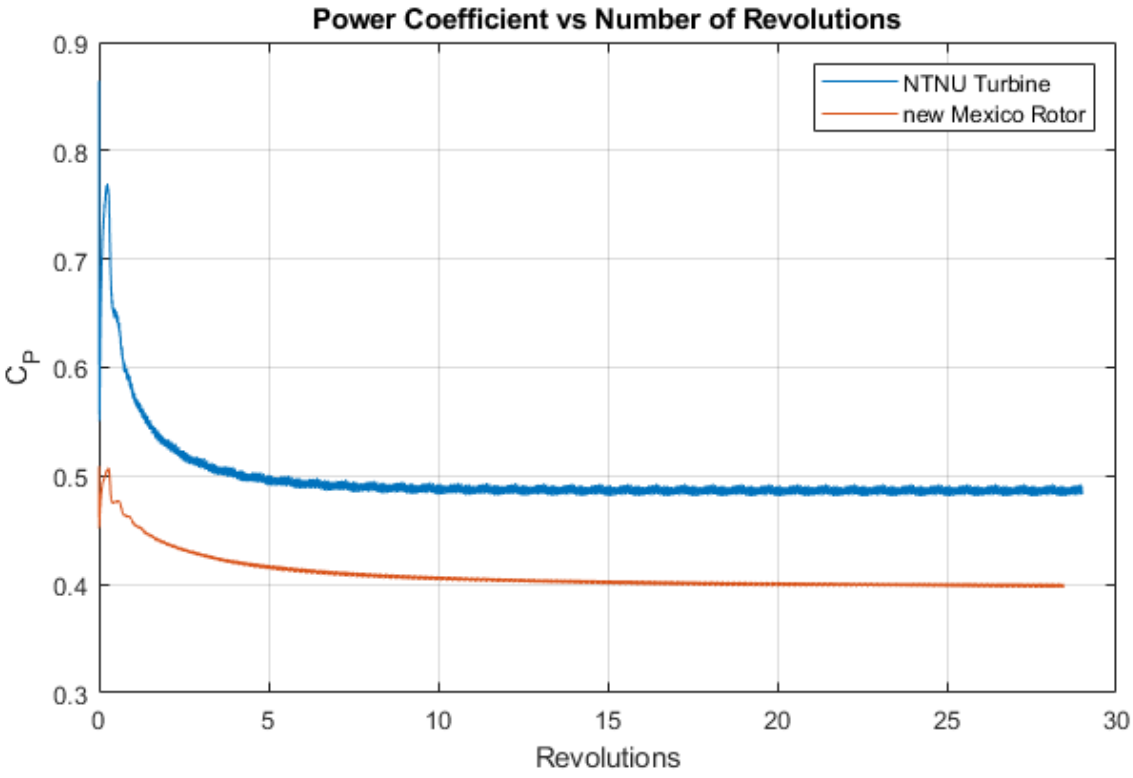

Figure 5-1 The number of rotations for the power coefficient C_p to become constant

However, the simulations for the NTNU rotor are performed at the optimal tip speed ratio $TSR = 6$ with wind speed $U_\infty = 10\ m/s$ giving the corresponding values of the tip speed $U_{tip} = 60\ m/s$ and rotational speed $\omega = 133.3\ rad/s$. Some simulations are performed by varying the TSR from 2 to 11 while keeping the inlet velocity at $10\ m/s$ to compare the results with the experimental result of Krogstad et al. [33].

The results are extracted after the power coefficient of the turbines reaches the constant value, as shown in Figure 5-1.

5.1.1 Time Step Size Selection

The studies have shown that the timestep chosen for ALM simulation should be constant throughout the runtime [21]. Initially, some studies are done to select the correct time step based on the number of timesteps needed for one revolution until the solution for power output converges [28]. However, most studies suggested that the timestep should be chosen so that the blade cannot pass more than one grid cell per time step in the rotor region [21, 26, 32]. In other words, it states that the Courant number at the tip of the blade should be equal to or less than 1. The Courant number at the tip is defined as

$$CFL_{tip} = \frac{U_{tip} \times \Delta t}{\Delta_{grid}} \tag{5.1}$$

In order to verify the time discretization, the simulations are performed by choosing various CFL_{tip} values by varying the time step. The variation of CFL_{tip} on the power output can be seen in Figure 5-2. The tip speed of the MEXICO rotor at the simulation condition is $U_{tip} = 100.2\ m/s$. It is evident from the graph that when the $CFL_{tip} = 1$, power starts to remain constant. The blade is now not traversing more than one grid cell per time step. The temporal discretization is only studied for the MEXICO rotor, as all the turbines should follow the same behavior. The rest of the simulations are performed corresponding to the value of $CFL_{tip} = 0.9$.

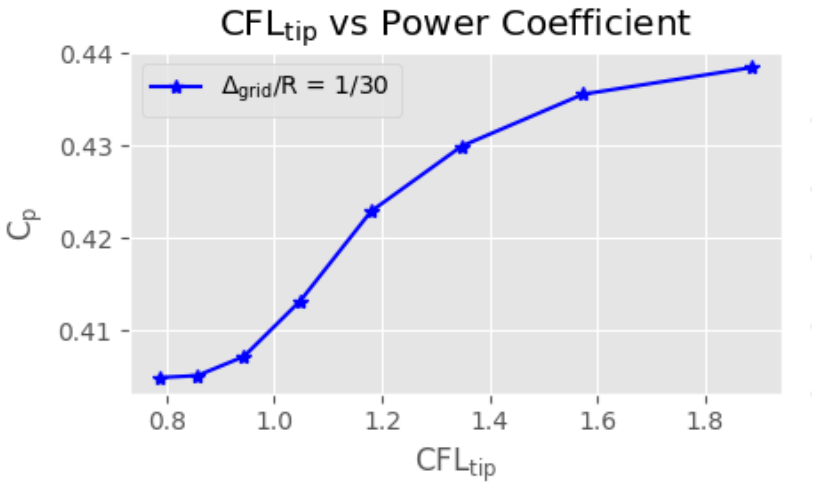

Figure 5-2 Variation in power coefficient to the tip courant number for MEXICO rotor

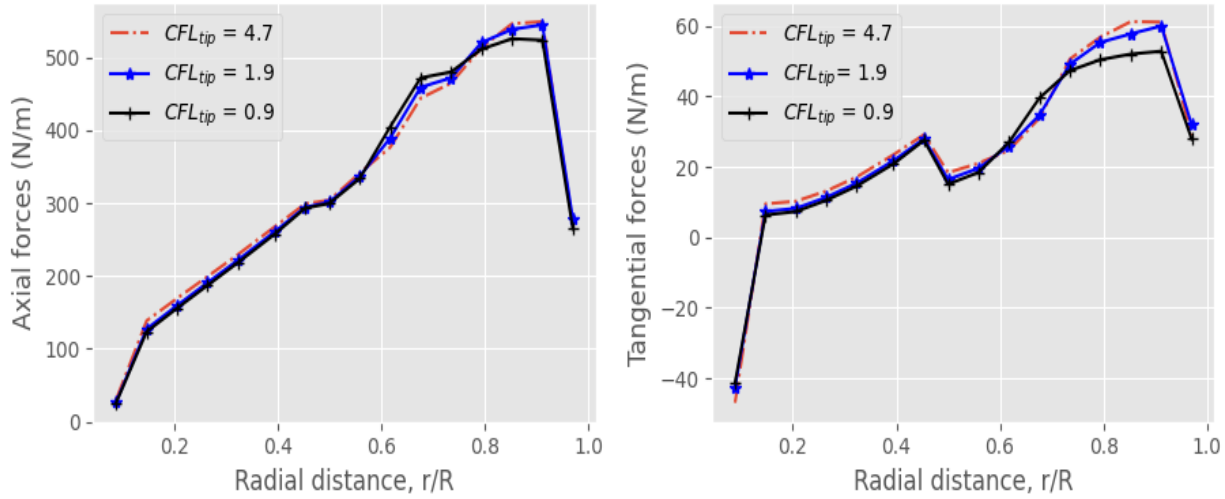

Figure 5-3 Variation of axial and tangential force distribution at various CFL_{tip} for the MEXICO rotor

The tangential and axial blade loading has also been analyzed for the time discretization study of the MEXICO rotor. Figure 5-3 shows the increased tangential blade loading near the blade tip for higher CFL_{tip} values. Moreover, blade loads are not smooth, and oscillations are present after 0.6 R blade distance, which reduces as the CLF_{tip} value decreases until it reaches less than 1. This behavior is observed because the speed of the blade is higher near the tip, and for the value of CFL_{tip} greater than one, the actuator points are crossing more than the size of the grid. The overprediction is present more at the blade tip in tangential loading.

5.1.2 ALM Simulation of MEXICO Rotor using Equivalent Elliptic Planform Method

The grid resolution is also the critical parameter for the actuator line method to predict blade loading accurately. In the guidelines mentioned by Jha et al. [21], the grid size Δ_{grid}/R should be in between bounds of 1/30 and 1/60 for the LES simulations, while the size of the actuator spacing should be such that $\Delta_p/\Delta_{grid} \geq 1.5$.

This section will validate the guidelines defined for the ALM parameters described in section 3.1.3. Figure 5-4 shows the simulation results for the sectional normal and tangential forces along the blades using the elliptic Gaussian radius method and grid size discretization mentioned in the guidelines of ALM parameters compared against the experimental data and CFD simulation results in DTU_EllipSys3D present in the Mexnext-III (Phase 3) report [34].

The MEXICO rotor is bigger and has a blade aspect ratio of = 15.5, larger than the NTNU model turbine. When the MEXICO rotor is divided into 17 ALM actuator points, the coarse grid of $\Delta_{grid}/R = 1/30$ results in $\Delta_p/\Delta_{grid} = 1.76$ while the finest grid of $\Delta_{grid}/R = 1/60$ results in $\Delta_p/\Delta_{grid} = 3.5$. The reference grid of $\Delta_{grid}/R = 1/30$ results in the value of $n_{max} = 3$ so that it satisfies $(n_{max}\,\Delta_{grid})/R = 0.1$ in equation (3.36), while for the finest grid $\Delta_{grid}/R = 1/60$ the $n_{max} = 6$. These values vary while keeping the parameter ε/c^* from equation (3.37) to a constant value of $\varepsilon/c^* = 1.22$. As the grid is refined, the time step size has also been reduced accordingly such that the actuator force shouldn't traverse more than one grid cell per timestep to satisfy the condition of $CFL_{tip} = 0.9$. Furthermore, for all the simulations, the minimum discretization criteria are such that $n_{min} = 1$.

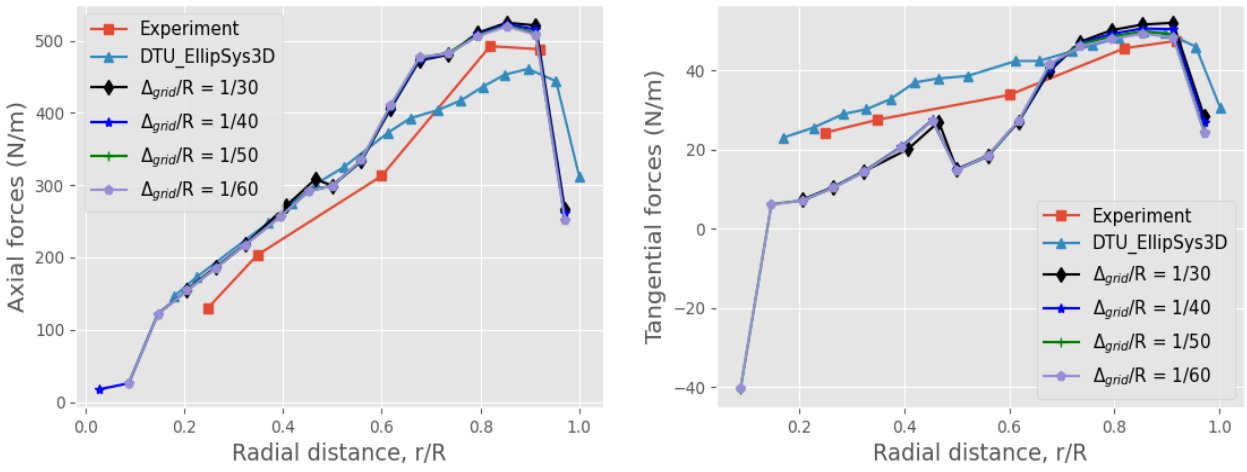

Figure 5-4 MEXICO rotor axial (left) and tangential forces (right) per unit span. ALM parameter: $\varepsilon/c^* = 1.22$, actuator points = 17

In Figure 5-4, even though the CFD simulation of DTU_Ellipse 3D under-predicts the normal loading and over-predicts the tangential loading, it is considered a good comparison for the results

in this study as data measured for the MEXICO rotor is not present near the blade tip. Figure 5-4 shows the blade's tip loading reduction for all the grid resolutions. Increasing the grid resolution to $\Delta_{grid}/R = 1/60$ results in the reduction of the loading near the blade tip as compared to the coarser grids. The sudden increase in tangential loading at mid-span is caused by the change of the DU91-W2-250 to the RISØ-A1-21 airfoil. An explanation for this anomaly can be linked to the interpolation of the chord in the ALM code. The computed results also show discrepancies throughout the blade compared to the measured data, which can be linked to inaccuracy in airfoil tables. The author extracted the airfoil data at the specific Reynolds numbers from the ECN phase 3 [41] report.

Table 5-1 below shows the power and thrust calculated for the MEXICO rotor. The increase in the grid refinement from $\Delta_{grid}/R = 1/30$ to $\Delta_{grid}/R = 1/60$ caused the percentage change in power from 0.11% to 2.2%. The difference in the power predicted by the ALM method is 7% less than in the experiment. In addition, CFD simulations of DTU_Ellipse3D drastically overpredicted the power by 11%, so the ALM method based on these parameters presented nearly accurate power prediction. However, the thrust has shown significant overprediction by 29% compared to the experimental results, which decreases with the increase in the grid refinement. Compared to the experimental results, the power and thrust are under-predicted and over-predicted, respectively, by the ALM method. Furthermore, the reduction in the power and thrust is evident with the decrease in the grid size parameter Δ_{grid}/R, which can be attributed to the reduction in the axial and tangential loading seen in Figure 5-4.

Table 5-1 Power and thrust of MEXICO Rotor. ALM parameters: $\boldsymbol{\varepsilon/c^{*} = 1.22}$ and actuator points = 17

MEXICO rotor	Power Coefficient (C_p)	Thrust Coefficient (C_T)	Power (W)	Thrust (N)
ALM: ($\Delta_{grid}/R = 1/30$)	0.402	1.027	13224	2249
ALM: ($\Delta_{grid}/R = 1/40$)	0.402	1.021	13209	2236
ALM: ($\Delta_{grid}/R = 1/50$)	0.398	1.019	13066	2232
ALM: ($\Delta_{grid}/R = 1/60$)	0.394	1.017	12933	2227
Experiment	0.434	0.790	14275	1731
DTU_Ellipse3D	0.480	0.800	15773	1753

Previously, the grid resolution comparison was made by keeping the number of actuator points to 17, which also increased the parameter such that $\Delta_p/\Delta_{grid} = 3.52$ for the finest grid resolution $\Delta_{grid}/R = 1/60$. Therefore, Figure 5-5 shows the effect of increasing grid resolution Δ_{grid}/R on blade loading while also increasing the number of actuator points such that the ALM parameter is kept constant at $\Delta_p/\Delta_{grid} = 1.7$. Overall, the results in Figure 5-5 have shown no significant difference. Therefore, the parameter criteria of $\Delta_p/\Delta_{grid} \geq 1.5$ maintains enough grid cells within the smearing to calculate the proper prediction of forces. The only difference in the reading for $\Delta_p/\Delta_{grid} = 1.7$ compared to $\Delta_p/\Delta_{grid} = 3.52$ when using same grid resolution $\Delta_{grid}/R = 1/60$ is that the jump becomes significant near the region of the airfoil change.

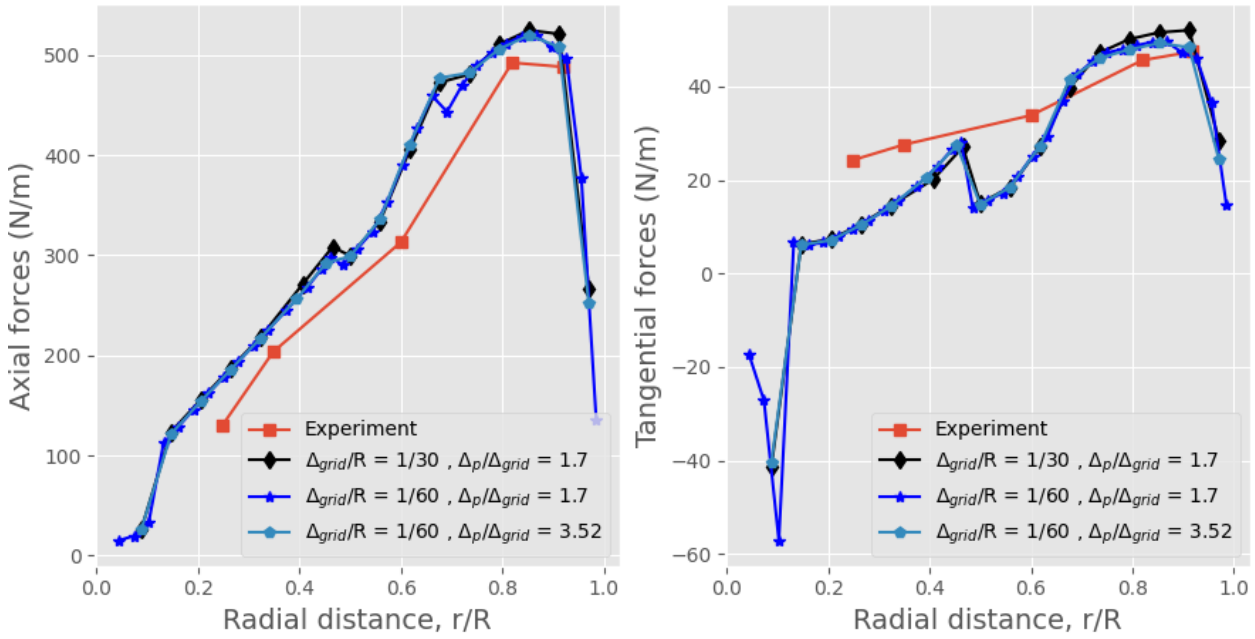

Figure 5-5 MEXICO rotor axial (left) and tangential forces (right) per unit span. ALM parameter: $\boldsymbol{\varepsilon/c^{*} = 1.22}$, $\boldsymbol{\Delta_p/\Delta_{grid} = 1.7}$ and $\boldsymbol{\Delta_p/\Delta_{grid} = 3.52}$

Table 5-2 compares the power and thrust from the rotor for the constant $\Delta_p/\Delta_{grid} = 1.7$ parameters, which is achieved by increasing the number of actuator points for grid resolution $\Delta_{grid}/R = 1/60$. The constant Δ_p/Δ_{grid} criterion has shown similar behaviour to what was observed previously. The grid resolution $\Delta_{grid}/R = 1/60$ showed both the reduction in power and thrust calculations as compared to $\Delta_{grid}/R = 1/30$. Important to note here that changing the parameter $\Delta_p/\Delta_{grid} = 3.52$ to $\Delta_p/\Delta_{grid} = 1.7$ while keeping the grid resolution $\Delta_p/\Delta_{grid} = 1/60$ resulted in less error in power and thrust prediction from 9.7% and 28.6% to 9.1% and 28%, respectively, compared to experimental results. With only a slight difference in results, the increased grid resolution and the increased number of actuator points for practical computation are difficult to justify as the requirement of computational power was raised by the magnitude of 4.

Table 5-2 Rotor power and thrust of MEXICO rotor; ALM parameters: $\varepsilon/c^* = 1.22$, $\Delta_p/\Delta_{grid} = 1.7$ and $\Delta_p/\Delta_{grid} = 3.52$

MEXICO rotor	Power Coefficient (C_p)	Thrust Coefficient (C_T)	Power (W)	Thrust (N)
ALM: $(\frac{\Delta_{grid}}{R} = \frac{1}{30}); \frac{\Delta_p}{\Delta_{grid}} = 1.7$	0.402	1.027	13224	2249
ALM: $(\frac{\Delta_{grid}}{R} = \frac{1}{60}); \frac{\Delta_p}{\Delta_{grid}} = 1.7$	0.394	1.011	12962	2215
ALM: $(\frac{\Delta_{grid}}{R} = \frac{1}{60}); \frac{\Delta_p}{\Delta_{grid}} = 3.52$	0.394	1.017	12933	2227

5.1.3 Comparison of Elliptic Gaussian Radius Method with Constant Mesh, Prandtl's Tip loss, and Chord-based Method for MEXICO Rotor

The MEXICO rotor simulations are also performed using other Gaussian radius methods: constant chord and constant mesh-based Gaussian radius with and without the inclusion of tip loss correction factor (Prandtl's Correction). This is done to analyze the effect of different Gaussian methods on the tangential and blade loading of the Mexico rotor. The results of blade loading due to these Gaussian radius methods are compared against the elliptic Gaussian radius. The constant mesh-based Gaussian radius is applied, similar to the Troldborg [19] findings, such that $\varepsilon/\Delta_{grid} = 2$. For the constant chord method, the value computed for the elliptic Gaussian radius using equation (3.37) is chosen for the constant chord Gaussian radius, i.e., $\varepsilon/c = 1.22$. It is done because the value of $\varepsilon/c = 0.25$ suggested by Shives and Crawford [20] requires a condition of $\varepsilon/\Delta_{grid} \geq 4$ which result in very fine grid not suitable for windfarm simulations.

Figure 5-6 shows interesting results near the blade tip loading using the various Gaussian radius methods. All the methods demonstrate the reduction in the blade loading at the tip. The constant

grid-based Gaussian radius can capture the loading reduction at the blade tip analogous to the elliptic Gaussian radius. The behavior of the constant grid-based method is in contrast to what was observed for the NTNU rotor (see section 5.2.5), where the blade loads are overpredicted at the blade tip. Similarly, the constant chord Gaussian radius depicts a similar trend. However, it overpredicts blade loading just at the tip. The similar behavior of constant chord and constant elliptic Gaussian radius can be seen in the paper of Jha et al. [21] when a 5 MW NREL turbine is used for the simulations. It is worth mentioning that the 5 MW NREL wind turbine and MEXICO rotor have higher AR than the NREL Phase six-rotor and NTNU turbine. Hence, the constant grid $\varepsilon/\Delta_{grid}$ and chord-based Gaussian radius ε/c , similar to the elliptic Gaussian radius ε/c^* , can accurately predict the tip blade loading for wind turbines having a high blade aspect ratio. Furthermore, when the Prandtl's tip loss correction is applied, the wind turbine loads are underpredicted near the blade tip compared to the experimental values supporting the fact that the tip loss correction is an artificial way of improving the tip loading in ALM simulations.

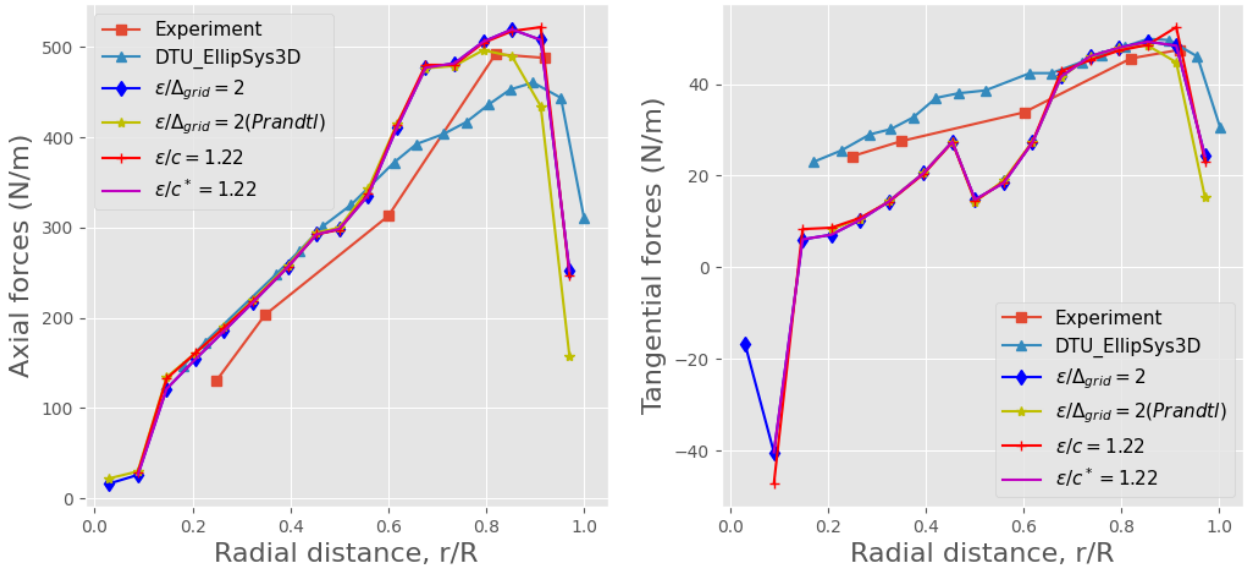

Figure 5-6 MEXICO axial (left) and tangential forces (right) per unit span. ALM parameters = $\Delta_{grid}/R = 1/60$

Table 5-3 shows that power and thrust computed using the constant grid and constant chord-based Gaussian radius are identical to the elliptic Gaussian radius ε/c^*. Conversely, the implementation of Prandtl's tip loss correction on the constant grid-based Gaussian radius resulted in an

underprediction of power by 14% compared to the measured value. Since, in the CFD simulations, the three-dimensional flow field fully resolves the blade and root tip vortices, inducing the tip loss correction is difficult to justify in the ALM framework, as it was initially developed for the BEM theory.

Table 5-3 Power and thrust for MEXICO rotor $U = 15\ m/s$ and $\lambda = 6.7$. ALM parameter: $\Delta_{grid}/R = 1/60$

MEXICO Rotor	Power Coefficient (C_p)	Thrust Coefficient (C_T)	Power (W)	Thrust (N)
ALM: $\varepsilon/\Delta_{grid} = 2$	0.399	1.02	13096	2230
ALM: $\varepsilon/\Delta_{grid} = 2$ (Prandtl)	0.369	0.99	12136	2170
ALM: $\varepsilon/c = 1.22$	0.401	1.03	13166	2266
ALM: $\varepsilon/c^* = 1.22$	0.394	1.02	12933	2227
Experiment	0.434	0.79	14275	1731

5.1.4 ALM simulation for NTNU Turbine using Equivalent Elliptic Planform Method

Similar to the previous section, this section will validate the guidelines for the ALM parameters described in section 3.1.3 but with the NTNU model turbine (smaller size and blade aspect ratio). The simulation results for the sectional normal and tangential blade forces using grid size discretization mentioned in the guidelines of ALM parameters compared against the measured data by Krogstad et al. [33].

The NTNU rotor has the aspect ratio $AR = 9.97$, much less than the MEXICO rotor. The coarse grid resolution is $\Delta_{grid}/R = 1/43$ for this rotor with the 28 actuator point such that $\Delta_p/\Delta_{grid} = 1.51$ satisfying the condition $\Delta_p/\Delta_{grid} \geq 1.5$ equating the corresponding $n_{max} = 4.3$ resulting in a constant ellipse value of $\varepsilon/c^* = 0.783$ from equation (3.37). Similarly, when the grid

resolution Δ_{grid}/R increases n_{max} also increases as described in equation (3.36) such that $\varepsilon/c^* = 0.783$. Therefore, it shows that the constant epsilon ε/c^* is the function of the blade aspect ratio. Similarly, the time step sizes are adjusted for every simulation such that $CFL_{tip} = 0.9$ keeping the actuator blade from traversing more than one grid cell per time step.

The computed turbine power and thrust coefficients are tested against the experimental result of Krogstad et al. [39] at varying tip speed ratios λ with the same inlet condition. The changing TSR values cause the change in blade tip speed; therefore, timestep sizes are again adjusted such that $CFL_{tip} = 0.9$. Figure 5-7 and Figure 5-8 show the variation of power and thrust coefficient with the TSR, respectively. The comparison is made between ALM's findings with the measured data hence validating the accuracy of the constant ellipse method for Gaussian smearing parameter $\varepsilon/c^* = constant$. The results are in excellent agreement with the measured data. The power coefficient is maximum at the $TSR = 5.8$, similar to what was observed in the original experiment. However, the author associates discrepancies in computed results and the measured data with the domain setup size chosen for simulation, which is equal to $3\ m$ in both lateral directions (y, z) in contradiction to the wind tunnel size in the lateral direction of $2.7\ m$ and $1.9\ m$ in y and z direction respectively. The domain setup size was changed to the same length in y and z so that the grading in the blockMesh dictionary can create the grid sizes with the unity aspect ratio (condition for isotropic turbulence in Smagorinsky LES simulations). In addition, the tower geometry is also excluded in the simulation and only includes the hub and rotor geometry.

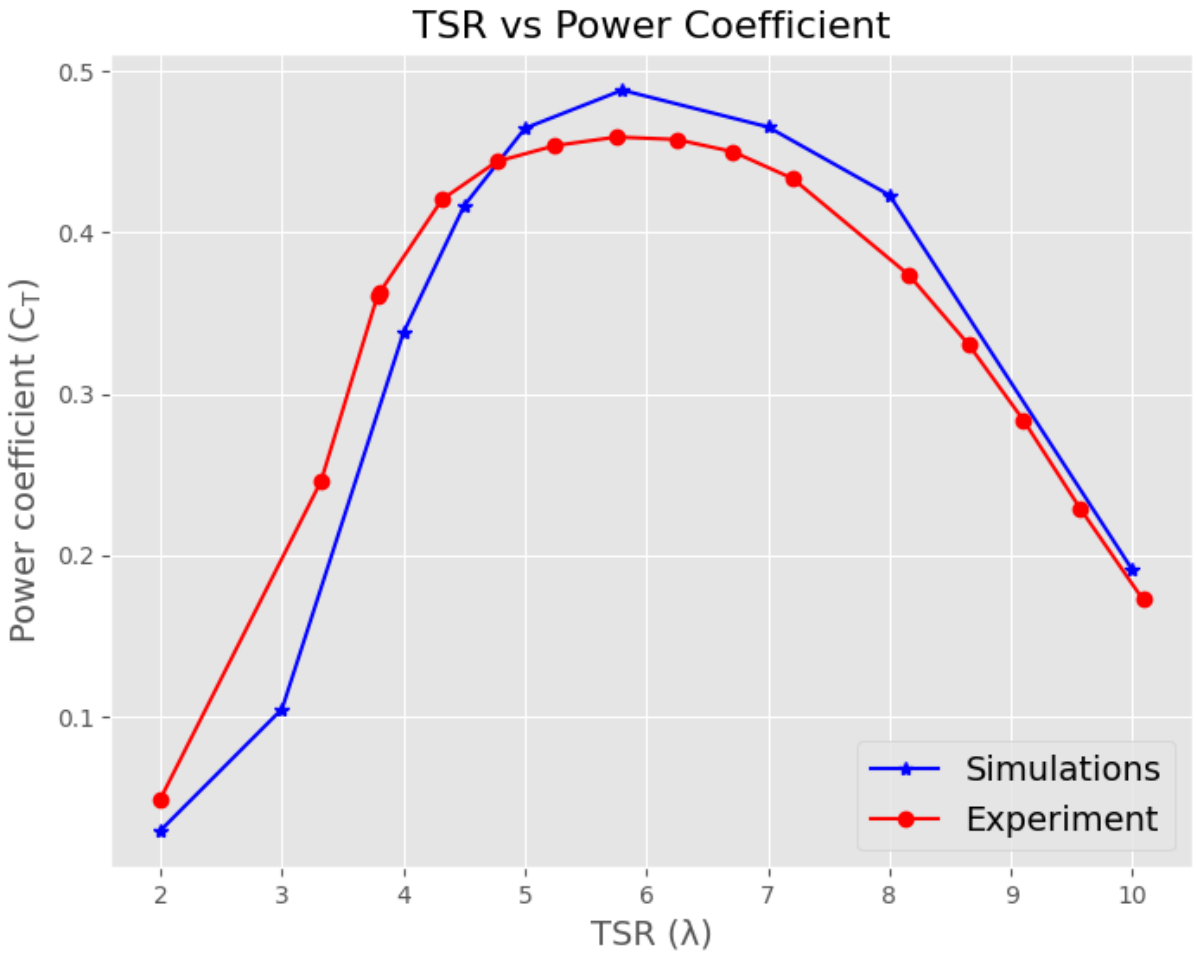

Figure 5-7 Power coefficient variation to tip speed ratio for NTNU wind turbine with wind speed $U = 10\ m/s$; ALM parameters: $\varepsilon/c^* = 0.783$, $\Delta_{grid}/R = 1/43$ and $\Delta_p/\Delta_{grid} = 1.51$

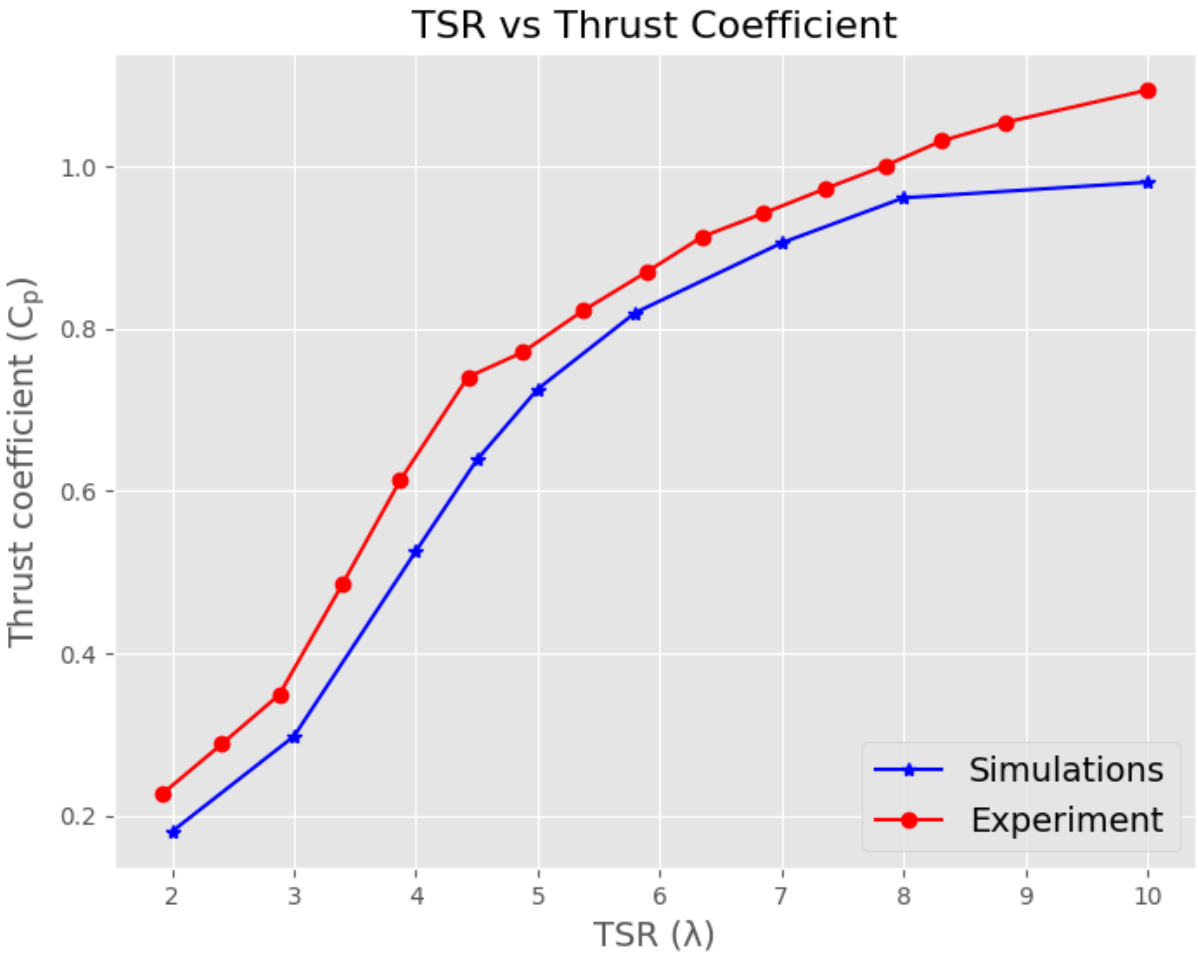

Figure 5-8 Thrust coefficient variation to tip speed ratio for NTNU wind turbine with wind speed $U = 10\ m/s$; ALM parameters: $\varepsilon/c^* = 0.783$, $\Delta_{grid}/R = 1/43$ and $\Delta_p/\Delta_{grid} = 1.51$

NTNU turbine lacks the experimental data for the normal and tangential spanwise forces. Therefore, this study presents the grid study without validation to the other sources and compares the axial and tangential spanwise blade forces based on the constant epsilon $\varepsilon/c^* = 0.783$ methods when the turbine runs at the optimal TSR value of $\lambda = 6$. Figure 5-9 shows the smooth loss of loading near the tip of the blade for grid resolution $\Delta_{grid}/R = 1/60$ in comparison to the grid resolution of $\Delta_{grid}/R = 1/43$. The forces near the blade tip show some discrepancy in results using the coarser grid resolution. In contrast, simulations of the MEXICO rotor show similar results at the tip loads for the grid resolution of 1/60 and 1/30, which can be attributed to the fact that the MEXICO rotor had a higher aspect ratio, i.e., epsilon is a function of aspect ratio.

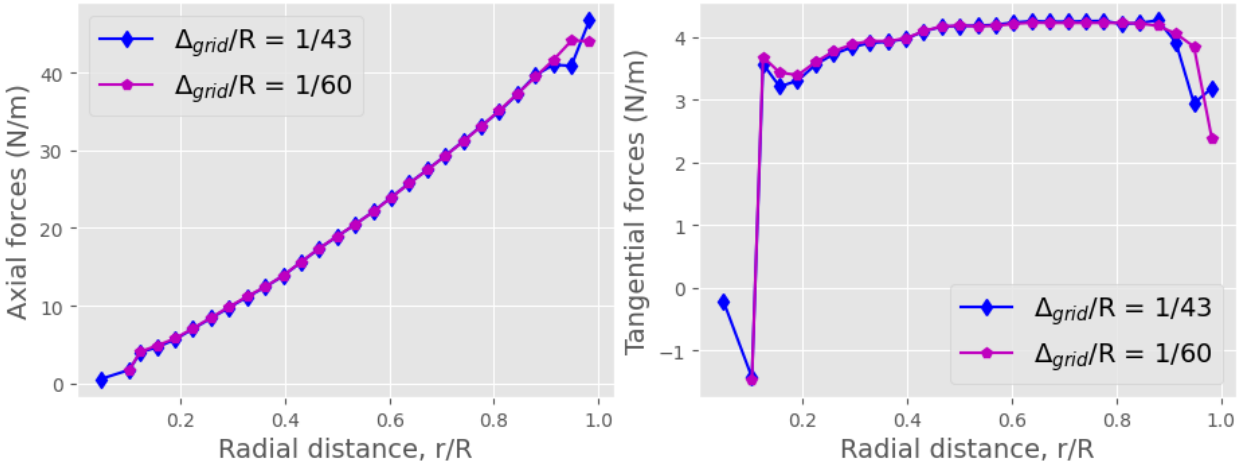

Figure 5-9 NTNU turbine axial (left) and tangential forces (right) per unit span $U = 10m/s$ and $\lambda = 6$. ALM parameter: $\varepsilon/c* = 0.783$, $\Delta_p/\Delta_{grid} = 1.51$ for $\Delta_{grid}/R = 1/43$ and $\Delta_p/\Delta_{grid} = 2.15$ for $\Delta_{grid}/R = 1/60$

Table 5-4 compares the measured and calculated power based on the grid resolution. The result shows the overprediction in computing power by 4.7% as compared to measured power for the grid resolution $\Delta_{grid}/R = 1/43$, which reduces to 4.1% when the grid resolution is increased to $\Delta_{grid}/R = 1/60$. The thrust coefficient also shows excellent agreement with the measured data.

Table 5-4 Rotor Power and Thrust for NTNU Turbine span $U = 10m/s$ and $\lambda = 6$. ALM parameters: $\varepsilon/c^* = 0.783$, $\Delta_p/\Delta_{grid} = 1.51$ for $\Delta_{grid}/R = 1/43$ and $\Delta_p/\Delta_{grid} = 2.15$ for $\Delta_{grid}/R = 1/60$

NTNU Turbine	**Power Coefficient (C_p)**	**Thrust Coefficient (C_T)**	**Power** (W)	**Thrust** (N)
ALM: $\Delta_{grid}/R = 1/43$	0.482	0.830	188	32.3
ALM: $\Delta_{grid}/R = 1/60$	0.480	0.831	187	32.4
Experiment	0.460	0.820	179	31.9

5.1.5 Comparison of Elliptic Gaussian Radius Method with Constant Mesh, Prandtl's Tip loss, and Chord-based Method for NTNU Turbine

This section will analyze and compare the results of Gaussian radius ε based on the constant chord method ε/c , constant grid method, and Prandtl's tip loss factor with the elliptical Gaussian radius ε/c^* method. For the constant grid base method, the Gaussian radius is chosen according to the Troldborg [19]findings of $\varepsilon/\Delta_{grid}= 2$. On the other hand, for the constant chord base method, the work of Shives and Crawford [20] suggests that a constant Gaussian radius should be selected such that $\varepsilon/c = 0.25$ and $\varepsilon/\Delta_{grid} \geq 4$, which requires a very fine grid of $\Delta_{grid}/R = 1/325$ for minimum chord size near the tip of a small NTNU turbine. The very fine grid refinement would result in high computational resources. Hence, the value computed for the elliptic Gaussian radius ε/c^* from equation (3.37) is selected for the constant chord method, i.e., $\varepsilon/c = 0.783$.

Figure 5-10 illustrates and compares the results of section forces for the constant grid-based Gaussian radius $\varepsilon = 2$ with and without using the Prandtl's tip loss factor and constant chord-based Gaussian radius $\varepsilon/c = 0.783$ with the elliptic Gaussian radius $\varepsilon/c^* = 0.783$. The findings are similar to those observed in Jha et al. [21] paper for the rotor with the small aspect ratio, i.e., $AR = 9.97$. Both tangential and axial loadings are overpredicted near the blade tip for grid-based and constant chord-based methods compared to the elliptic Gaussian radius. Hence, the grid-based and constant chord-based methods cannot resolve the tip vortices for the NTNU-rotor. On the other hand, Prandtl correction under-predicts the blade tip load compared to the elliptic Gaussian radius. Hence, the power and thrust coefficient values are also under-predicted compared to the experimental findings when Prandtl's correction is applied to the grid-based Gaussian radius, as seen in Table 5-5. This supports the idea that Prandtl's tip loss correction is an artificial way of improving the blade tip loads when using the constant Gaussian radius in ALM simulations.

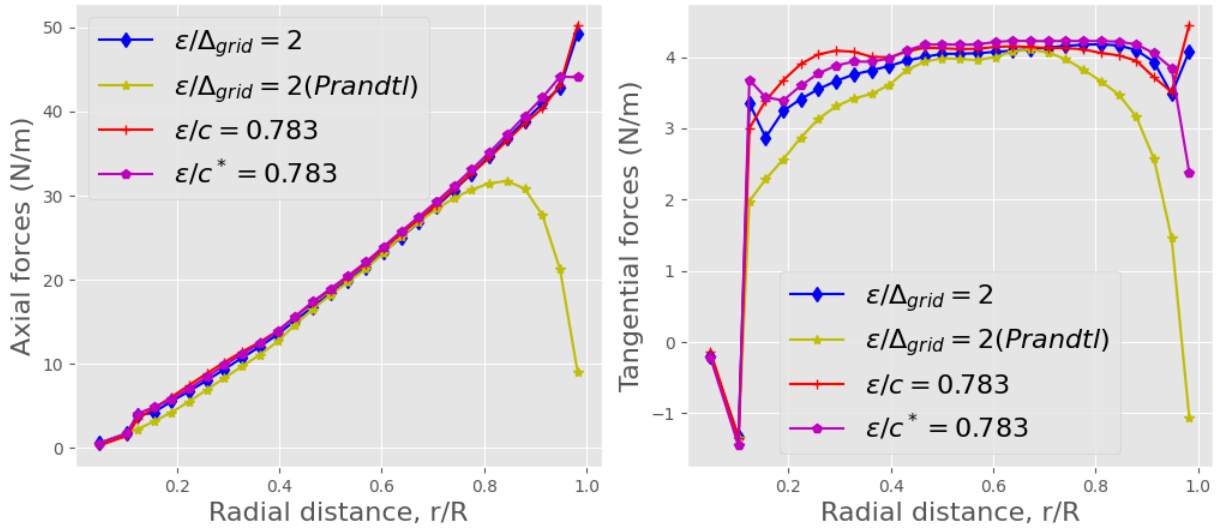

Figure 5-10 Axial (left) and tangential forces (right) per unit span $U = 10\ m/s$ and $\lambda = 6$ for the NTNU turbine. ALM parameters: $\Delta_{grid}/R = 1/60$

The results in Table 5-5 show that the elliptic Gaussian radius predicted the closest result to the experimental finding. However, constant-chord and grid-based Gaussian radius predicted higher power than experimental findings, which is due to higher blade loading acting near the blade tip shown in Figure 5-10. When Prandtl's tip loss correction is applied on the grid-based Gaussian radius ε, the result shows a reduction in the predicted value of power and thrust by 17% and 18%, respectively, compared to the measured data. Therefore, it proves the notion that tip-loss correction is an artificial way of improving the blade tip loads in BEM simulations that has no justification in ALM simulations where blade fields are fully resolved.

Table 5-5 Power and thrust for NTNU turbine $U = 10m/s$ and $\lambda = 6$. ALM parameters: $\Delta_{grid}/R = 1/60$

NTNU Turbine	Power Coefficient (C_p)	Thrust Coefficient (C_T)	Power (W)	Thrust (N)
ALM: $\varepsilon/\Delta_{grid} = 2$	0.482	0.822	188	32.0
ALM:$\varepsilon/\Delta_{grid} = 2$ (Prandtl)	0.380	0.67	148	26.1
ALM: $\varepsilon/c = 0.783$	0.486	0.845	189	32.9
ALM: $\varepsilon/c^* = 0.783$	0.480	0.831	187	32.4
Experiment	0.460	0.820	179	31.9

5.2 Multi-rotors Simulation based on Corrected ALM Parameters

This section analyses the multi-rotor system based on the parameters studied in the previous case. The MEXICO rotor is used for the multi-rotor study, and the Gaussian radius for actuator force smearing is defined by constant ellipse ε/c^* method as done in the previous section for the MEXICO rotor. Moreover, the near wake characteristics of the multi-rotor have been analyzed in comparison to the single-rotor for the $\Delta_{grid}/R = 1/30$.

5.2.1 The Grid Study Comparison of Multi-rotors

The previous method for the grid discretization is suitable for the single rotor wind turbines or the wind turbines in the tandem position. However, using the same grid discretization of $\Delta_{grid}/R = 1/30$ to model the multi-rotor side by side will result in only three grid points for the rotor spacing of $0.1\ D$. The three grid points may seem a little insufficient considering the high velocity and vorticity interaction occurring in the confined space when the two rotors pass each other. Therefore, a grid study has been done for the multi-rotor system to determine if the grid

discretization of $\Delta_{grid}/R = 1/30$ is sufficient to model the multi-rotor by comparing the result with the grid resolution of $\Delta_{grid}/R = 1/60$, which has six grid points in between the region.

Figure 5-11 shows the axial velocity magnitude between the two rotors as it varies in the lateral direction ($x = 0, z = 0$ with rotor center at $x = 0$, $z = 0$ and $y = \pm 2.475$) for the two grid resolution. The results show a difference in normalized axial velocity magnitude for the two grid resolutions near the blades. Similarly, the difference in velocity magnitude can be seen in the middle of the rotor when velocity samples are taken in the z-direction at the mid-distance ($y = 0$) of the two rotors in Figure 5-12, which is less chaotic than observed in the y-direction in Figure 5-11. Therefore, it becomes necessary to analyze near wake velocity to determine whether the grid size will significantly change the wake results. Figure 5-13 shows the normalized axial velocity at hub height sampled in the y-direction at a near wake length of $0.1\,D$. There is no significant difference in the near wake velocities seen in Figure 5-13. Therefore, the results show that it is sufficient to analyze the wakes of the multirotor with a coarse grid having three grid cells between the adjacent wind turbine rotors.

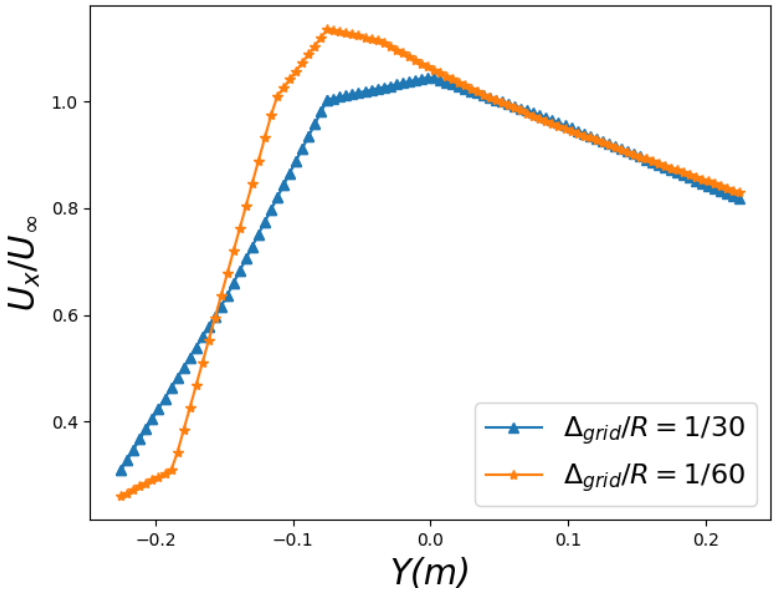

Figure 5-11 Normalized velocity magnitude between the two adjacent MEXICO rotors at hub height ($x = 0$ and $z = 0$)

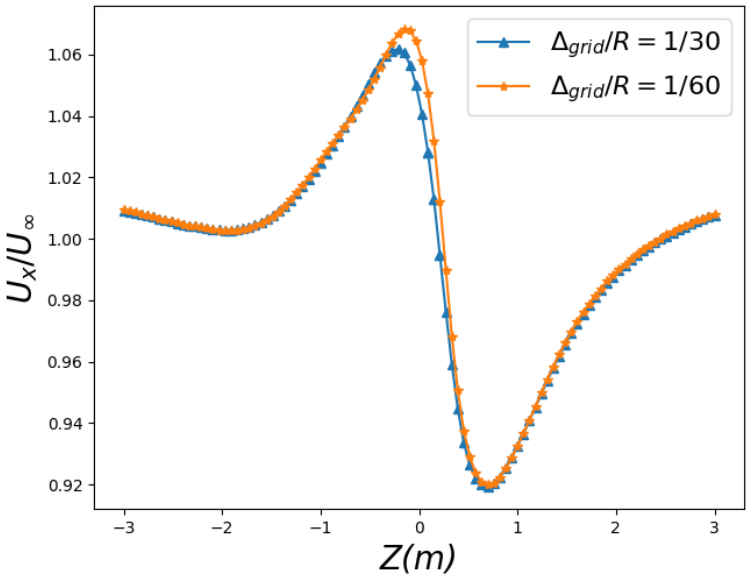

Figure 5-12 Normalized axial velocity magnitude varies with the height (z) between the two adjacent MEXICO rotors ($x = 0$ and $y = 0$)

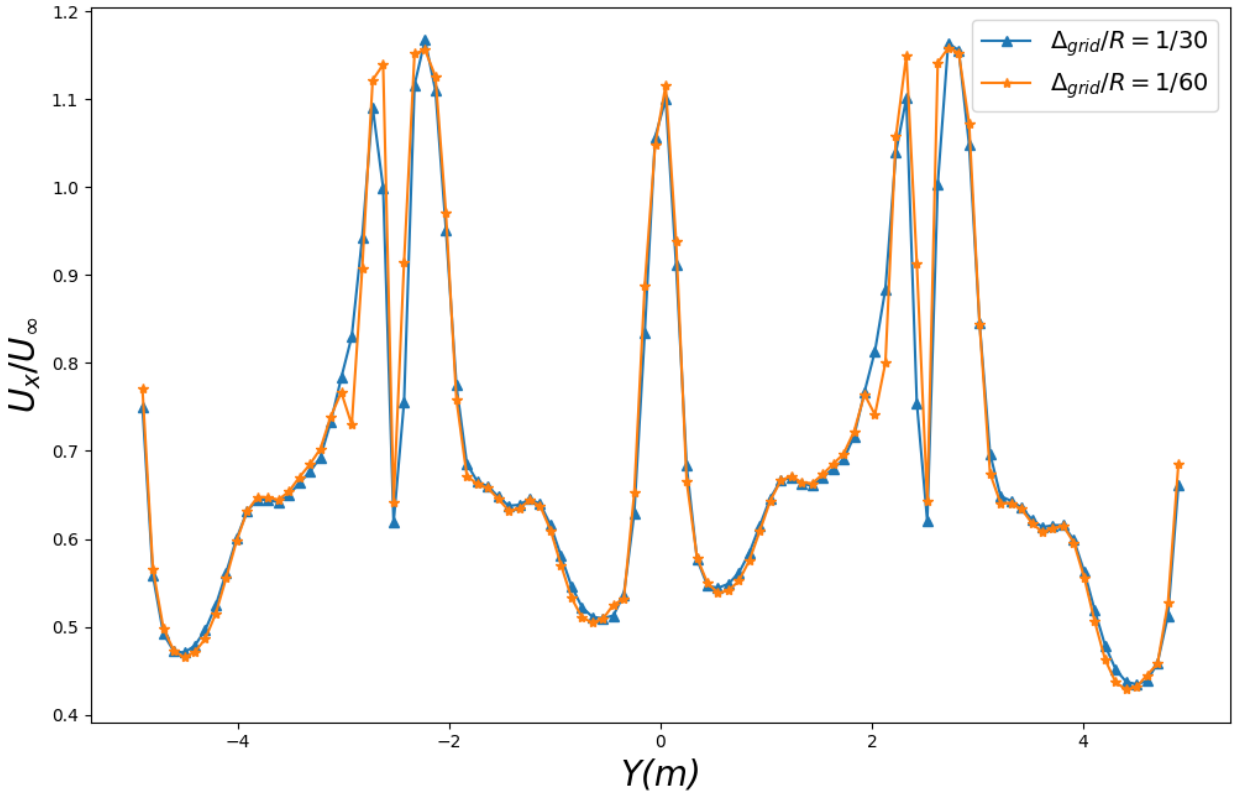

Figure 5-13 Profile of normalized axial velocity of two MEXICO rotors at downstream distance $x = 0.1\,D$ at the hub height ($z = 0$)

5.2.2 Comparison of Single and Multi-rotors

The next step is to compare the wake velocities of the single rotors with the multi-rotors. From Figure 5-14, it can be analyzed that for the single rotor at any downstream distance, the downstream wind velocity magnitude decreases at the back of the hub. When moving towards the blade tip from the hub, the downstream wind velocity increases near the blade's root, then decreases up to the blade's tip and suddenly increases more than the free stream velocity outside the rotor vicinity. At the near wake ($x = 0.1D$), the magnitude of the wind at the hub is very low, which increases downstream ($x = 2D$). On the other hand, there is a reduction in the velocity magnitude as wind progresses downstream in the vicinity of the blades. This behavior can be explained by the high vortices generated at the back of the hub. The low velocity always occurs at the center of the hub in the vicinity of the rotor.

However, the multi-rotor depicts the contrasting results in Figure 5-15. The velocity magnitude is very high in the middle of the two rotors, which decreases downstream. Interestingly, the wind velocity magnitude in the multi-rotor is not symmetrical about the hub as opposed to the single rotor case. The explanation for this behavior can be explained by Bernoulli's equation, as a very high velocity generated at the middle of the rotor causes a change in the pressure resulting in the movement of high-speed wind or, in other words, wake mixing. As a result, the quicker mixing causes overall wind velocity to be higher at a downstream distance $x = 2D$ compared to the single rotor. It is an interesting finding since the more rapid wake recovery observed in the two-rotors case can lead to a shorter distance for the placement of the downstream wind turbine, which in current practice is placed at about the distance of $10\ D$ downstream due to wake effects. The better illustrations of the tip vortices and wake structures for the single-rotor and multi-rotor cases are present in Figure 5-16 and Figure 5-17. The vortices are generated at the root and blade tip. Figure 5-17 confirms the presence of high velocities and eddies at the spacing between the two rotors of the multi-rotor case.

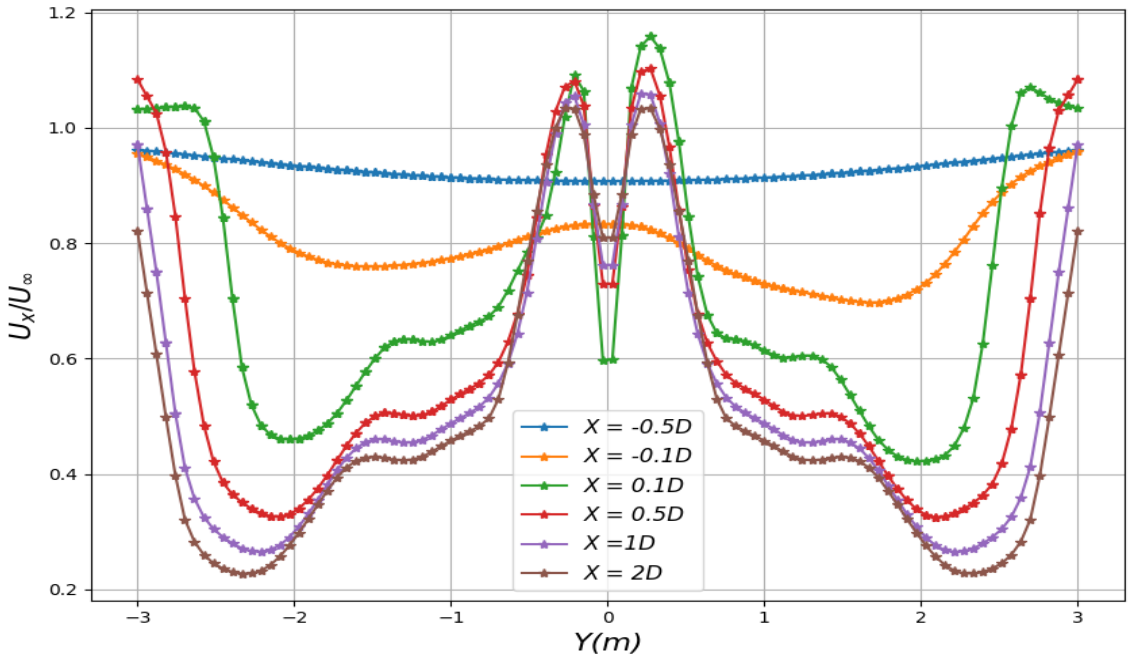

Figure 5-14 Normalised axial velocity profile at hub height for two upstream and four downstream locations of the single MEXICO rotor. $U_\infty = 15\ m/s$ ALM parameters: $\Delta_{grid}/R = 1/30$

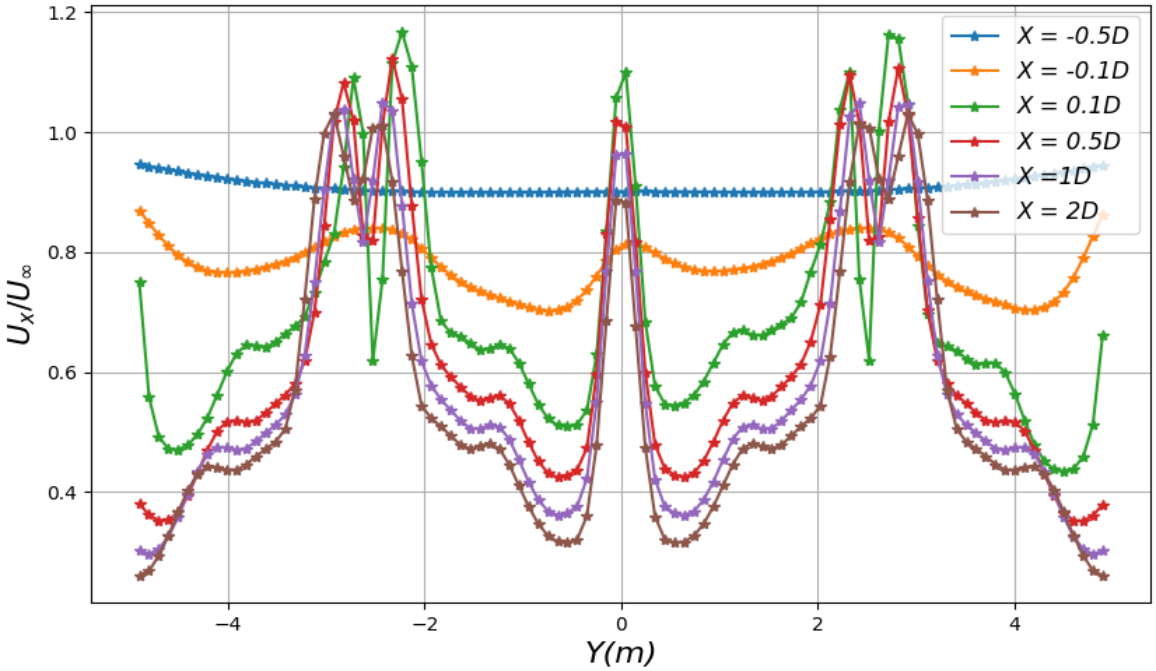

Figure 5-15 Normalised axial velocity profile at hub height for two upstream and four downstream locations of the two MEXICO rotors side by side. $U_\infty = 15\ m/s$ ALM parameters: $\Delta_{grid}/R = 1/30$

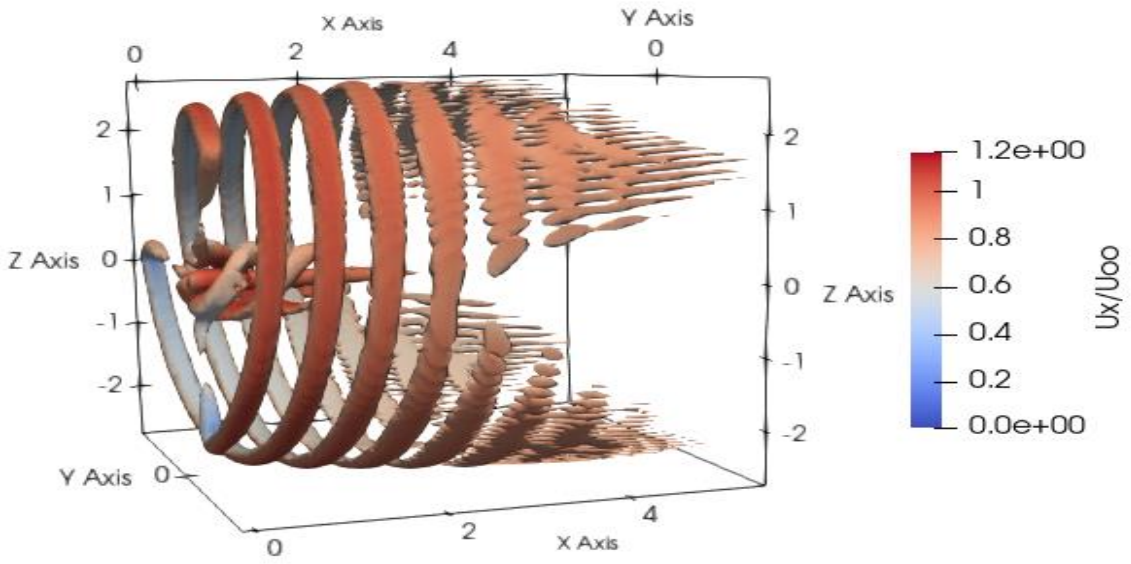

Figure 5-16 Wake structure and strength of a single rotor, an iso contour plot of vorticity magnitude 35 s^{-1} colouring by normalised axial velocity

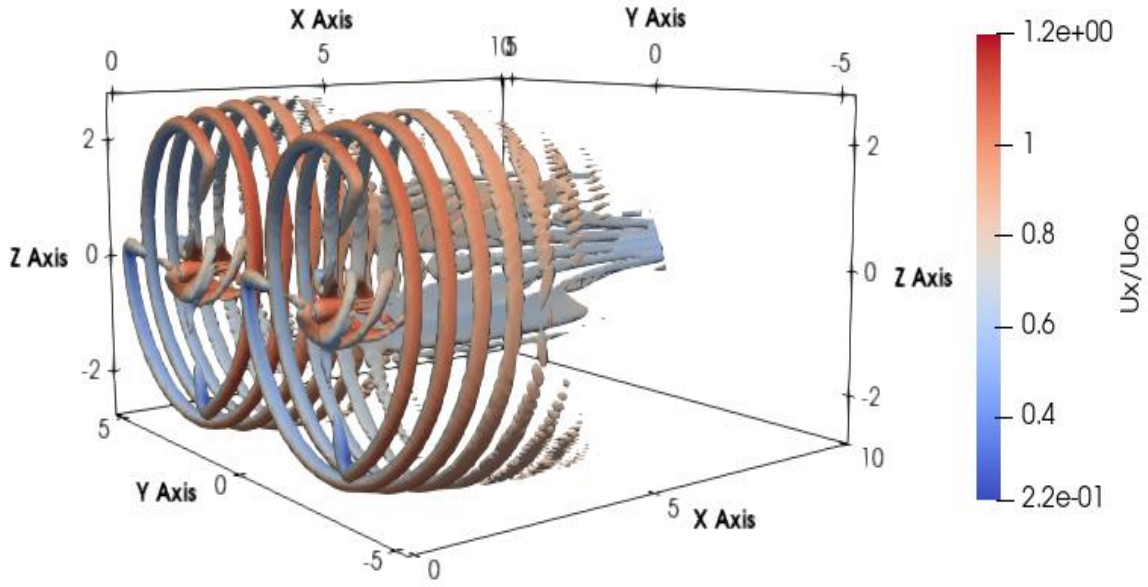

Figure 5-17 Wake structure and strength of two rotors, an iso contour plot of vorticity magnitude 35 s^{-1} colouring by normalised axial velocity

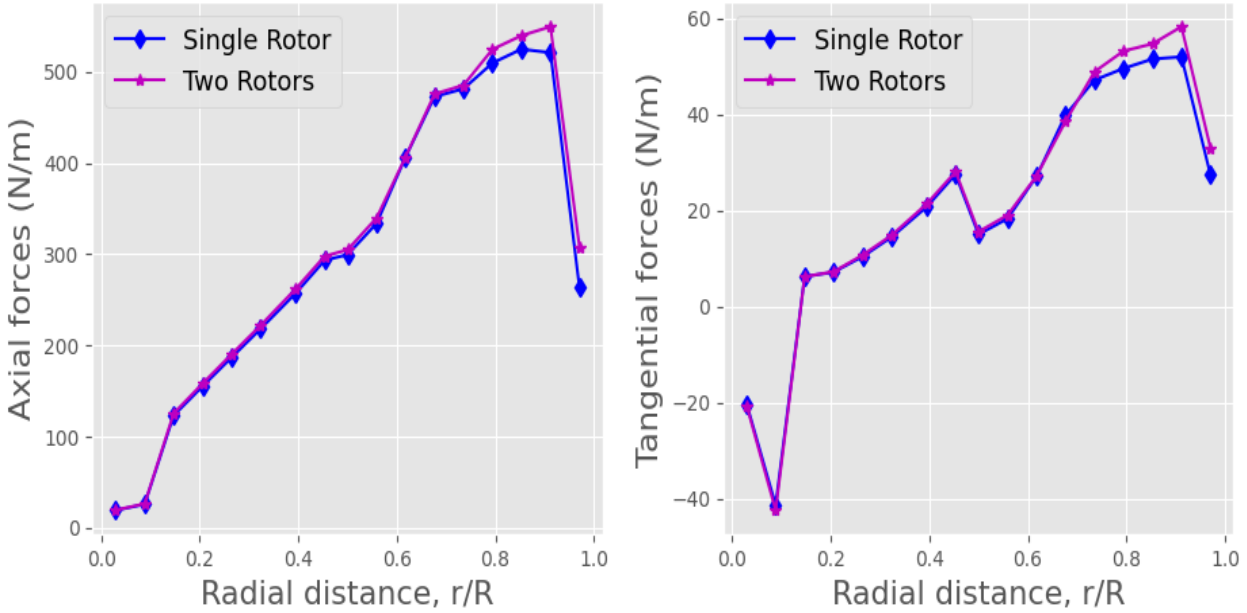

Figure 5-18 Axial and tangential forces per unit span for the MEXICO single and multi-rotor. ALM parameter: $\boldsymbol{\varepsilon/c^* = 1.22, \Delta_{grid}/R = 1/30}$

The results show interesting power output and blade loading findings when the two rotors are simulated. Table 5-6 shows the increase in power and thrust by 4% and 1%, respectively, compared to a single rotor. Similar findings in power and thrust were observed in the experiment of the Vestas multi-rotor system [29]. On the other hand, the magnitude of blade tip loadings increased by almost 2%, as seen in Figure 5-18. The increase in loading is due to the high wind velocity generated between the two rotors. Figure 5-19 gives the power comparison of single and multi-rotor systems visually.

Table 5-6 Rotor power and thrust for single and two rotors; ALM parameters: $\varepsilon/c^* = 1.22\ s$

ALM: $\varepsilon/c^* = 1.22$ $\Delta_{grid}/R = 1/30$	**Power Coefficient (C_p)**	**Thrust Coefficient (C_T)**	**Power (W)**	**Thrust (N)**
Single Rotor	0.402	1.027	13224	2248.9
Two Rotors	0.419	1.035	13753	2266.7

Finally, it is essential to mention here that the two rotors simulated have the same tip speed ratio, and their angular rotations are also synchronized with each other; in other words, both rotate exactly by the same degree at each increment of time. However, in reality, the two turbines will not be synchronized and may depict different behavior.

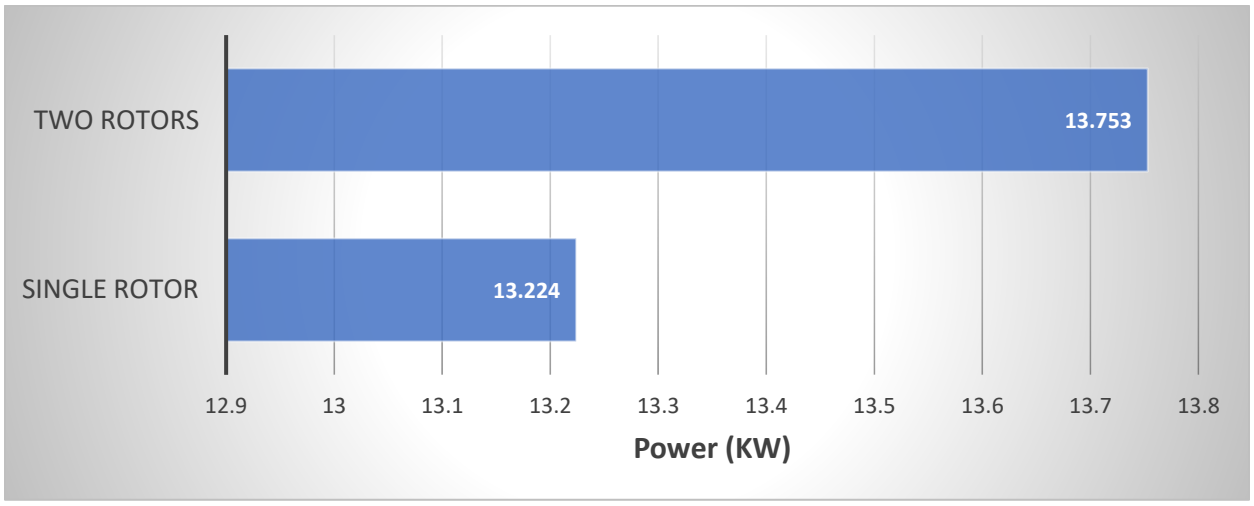

Figure 5-19 Power comparison of a single rotor with two rotors

CHAPTER 6 CONCLUSION

The ALM simulations of two model wind turbines, namely the NTNU model wind turbine and the MEXICO rotor, having different sizes and aspect ratios, are presented in the paper. The thesis consists of two parts. The first part includes the ALM parameters study, i.e., Gaussian radius, Grid resolution, timestep size, and actuator spacing, on the single wind turbine for LES simulations. The second part includes the simulation of the multi-rotor wind turbine in the ALM framework.

The comparison of spanwise force distribution on blades of the wind turbine using the three methods of Gaussian radius ε, namely, the constant chord ε/c method, the constant grid $\varepsilon/\Delta_{grid}$ method, and the elliptical Gaussian radius ε/c^* method gave almost similar results for the MEXICO rotor, while different results for the NTNU rotor. The over prediction in the blade tip loading is observed for the constant mesh and chord-based Gaussian radius but not for the elliptic Gaussian radius in the NTNU rotor simulation. The MEXICO rotor blade has a higher AR than the NTNU rotor. In summary, the three Gaussian methods can accurately predict the blade tip loading for the wind turbines with the higher AR, but for the wind turbines with low AR, better blade loading results are obtained when using the elliptic Gaussian radius method ε/c^* rather than the constant Gaussian radius methods that over-predict the tip load. The use of Prandtl's tip loss factor resulted in the underprediction of wind turbine power and blade tip loading for both the turbines compared to experimental results.

In the multi-rotor case, the finding suggested that grid resolution used for a single rotor can be used for the multi-rotor system for ALM-LES simulations. The power, thrust, and blade loading from each rotor increased by 4%, 1%, and 2%, respectively, compared to the single rotor when the multi-rotor simulations were performed by simulating two rotors side by side, having a $0.1\,D$ distance between them. In addition, the normalized axial velocity up to $2\,D$ distance showed higher velocity generation between the two rotors resulting in a more mixing and less velocity deficit than the single rotor.

6.1 Future Works

The two-rotors simulated side by side in the uniform inflow condition have the same tip speed ratio, and their angular rotations are also synchronized. Future work should include the asynchronous simulation of a multi-rotor system. Moreover, only two rotors are simulated side by side in the present case, but the multi-rotor consists of many rotors. One example is the Vestas multi-rotor [29], composed of four rotors in the inline arrangement. Therefore, the top and bottom rotors in a turbine multi-rotor comprising four rotors will depict a different behavior in the shear inflow conditions compared to the side-by-side rotors. Hence, the large eddy simulation of a four-rotor using the actuator line method (ALM) in sheared inflow conditions will give better turbine power and blade load predictions than the uniform inflow condition used in the present case.

REFERENCES

[1] "International Energy Agency," [Online]. Available: https://www.iea.org/data-and-statistics/data-browser?country=WORLD&fuel=Energy%20consumption&indicator=TFCbySource.

[2] "United Nations Framework Convention on Climate Change," the-paris-agreement, [Online]. Available: https://unfccc.int/process-and-meetings/the-paris-agreement/the-paris-agreement.

[3] "International Energy Agency," 2021. [Online]. Available: https://www.iea.org/reports/wind-power.

[4] "International Energy Agency," [Online]. Available: https://www.iea.org/fuels-and-technologies/renewables.

[5] T. Stehly and P. Duffy, "2020 Cost of Wind Energy Review," National Renewable Energy Laboratory, CO, 2021.

[6] J. N. Sørensen, W. Z. Shen and X. Munduate, "Analysis of wake states by a full-field actuator disc model," *Wind Energy*, vol. 1, no. 2, pp. 73 - 88, 1998.

[7] C. Leclerc and C. Masson, "Toward Blade-Tip Vortex Simulation with an Actuator-Lifting Surface Model," 2004.

[8] C. Leclerc and C. Masson, "Wind Turbine Performance Predictions Using a Differential Actuator-Lifting Disk Model," *Journal of Solar Energy Engineering*, vol. 127, 2005.

[9] P.-E. M. Réthoré, N. N. Sørensen and F. Zahle, "Validation of an Actuator Disc Model," in *European Wind Energy Association (EWEA)*, Warsaw, 2010.

[10] H. Glauert, "Airplane Propellers," in *Aerodynamic Theory: A General Review of Progress Under a Grant of the Guggenheim Fund for the Promotion of Aeronautics*, Springer Berlin Heidelberg, 1935, pp. 169--360.

[11] G. D. Yang, Z. Li, J. Qin and X. Yang, "Predictive capability of actuator disk models for wakes of different wind turbine designs," *Renewable Energy,* vol. 188, pp. 269-281, 2022.

[12] T. Revaz and F. Porté-Agel, "Large-Eddy Simulation of Wind Turbine Flows: A New Evaluation of Actuator Disk Models," *Energies,* vol. 14, no. 13, 2021.

[13] R. J. Stevens, L. A. Martínez-Tossas and C. Meneveau, "Comparison of wind farm large eddy simulations using actuator disk and actuator line models with wind tunnel experiments," *Renewable Energy,* vol. 116, pp. 470-478, 2018.

[14] P. Chasapogiannis, J. Prospathopoulos, S. Voutsinas and P. K. Chaviaropoulos, "Analysis of the aerodynamic performance of the multi-rotor concept," in *Journal of Physics: Conference Series*, 2014.

[15] J. N. Sørensen and W. Z. Shen, "Numerical modeling of wind turbine wakes," *Journal of Fluids Engineering,* vol. 124, no. 2, pp. 393-399, 2002.

[16] P. Å. Krogstad and P. E. Eriksen, "“Blind test” calculations of the performance and wake development for a model wind turbine," *Renewable Energy,* vol. 50, pp. 325-333, 2013.

[17] C. Archer, S. Mirzaeisefat and S. Lee, "Quantifying the sensitivity of wind farm performance to array layout options using large-eddy simulation," *Geophysical Research Letters,* vol. 40, no. 18, pp. 4963-4970, 2013.

[18] M. Tabib, A. Rasheed and T. Kvamsdal, "LES and RANS simulation of onshore bessaker wind farm: analysing terrain and wake effects on wind farm performance," *Journal of Physics: Conference Series,* vol. 625, 2015.

[19] N. Troldborg, "Actuator line modeling of wind turbine wakes," 2009.

[20] M. Shives and C. Crawford, "Mesh and load distribution requirements for actuator line CFD simulations," *Wind Energy,* vol. 16, no. 8, pp. 1183-1196, 2013.

[21] P. Jha, M. Churchfield, P. Moriarty and S. Schmitz, "Guidelines for Volume Force Distributions Within Actuator Line Modeling of Wind Turbines on Large-Eddy Simulation-Type Grids," *Journal of Solar Energy Engineering,* vol. 136, p. 031003, 08 2014.

[22] P. K. Jha and S. Schmitz, "Actuator curve embedding – an advanced actuator line model," *Journal of fluid mechanics,* vol. 834, 2018.

[23] P. Schito and A. Zasso, "Actuator forces in CFD: RANS and LES modeling in OpenFOAM," *Journal of Physics: Conference Series,* vol. 524, p. 012160, 2014.

[24] L. A. Martinez-Tossas, M. J. Churchfield and C. Meneveau, "Optimal smoothing length scale for actuator line models of wind turbine blades," *Wind Energy,* vol. 20, no. 6, pp. 1083-1096, 2017.

[25] L. A. Martínez Tossas and C. Meneveau, "Filtered lifting line theory and application to the actuator line model," *Journal of Fluid Mechanics,* vol. 863, pp. 269-292, 2019.

[26] M. Draper and G. Usera, "Evaluation of the Actuator Line Model with coarse resolutions," *Journal of Physics: Conference Series,* vol. 625, 2015.

[27] J. N. Sørensen, R. F. Mikkelsen, D. S. Henningson, S. Ivanell, S. Sarmast and S. J. Andersen, "Simulation of wind turbine wakes using the actuator line technique," *Philosophical transactions. Series A, Mathematical, physical, and engineering sciences,* vol. 373, no. 2035, 2015.

[28] P. Bachant, A. Goude and M. Wosnik, "Actuator line modeling of vertical-axis turbines," 2016.

[29] M. P. van der Laan, S. J. Andersen, N. Ramos García, N. Angelou, G. R. Pirrung, S. Ott, M. Sjöholm, K. H. Sørensen, J. X. Vianna Neto, M. Kelly, T. K. Mikkelsen and G. C. Larsen, "Power curve and wake analyses of the Vestas multi-rotor demonstrator," *Wind Energy Science,* vol. 4, pp. 251-271, 2019.

[30] N. S. Ghaisas, A. S. Ghate and S. K. Lele, "Effect of tip spacing, thrust coefficient and turbine spacing in multi-rotor wind turbines and farms," *Wind Energy Science,* vol. 5, no. 1, pp. 51-72, 2020.

[31] M. O. Hansen, Aerodynamics of Wind Turbines: second edition, Earthscan, 2008.

[32] P. Jha, M. Churchfield, P. Moriarty and S. Schmitz, "Accuracy of State-of-the-Art Actuator-Line Modeling for Wind Turbine Wakes," in *51st AIAA Aerospace Sciences Meeting including the New Horizons Forum and Aerospace Exposition,* 2013.

[33] P.-Å. Krogstad and M. S. Adaramola, "Performance and near wake measurements of a model horizontal axis wind turbine," *Wind Energy,* vol. 15, no. 5, pp. 743-756, 2012.

[34] J. Schepers, T. Lutz, K. Boorsma, S. Gomez-Iradi, I. Herraez, L. Oggiano, H. Rahimi, P. Schaffarczyk, G. Pirrung, H. A. Madsen and others, "Final Report of IEA Wind Task 29 Mexnext (Phase 3)," 2018.

[35] P. Bachant, A. Goude, daa-mec and M. Wosnik, "turbinesFoam/turbinesFoam: v0.1.1," Zenodo, 2019.

[36] P.-Å. Krogstad and P. E. Eriksen, ""Blind test" Workshop," 2011.

[37] J. Smagorinsky, "General circulation experiments with the primitive equations: I. The basic experiment," *Monthly weather review,* vol. 91, pp. 99-164, 1963.

[38] P. Bachant, "Github," 2018. [Online]. Available: https://github.com/turbinesFoam/turbinesFoam/wiki/Actuator-line-geometry.

[39] P.-Å. Krogstad and J. A. Lund, "An experimental and numerical study of the performance of a model turbine," *Wind Energy,* vol. 15, no. 3, pp. 443--457, 2012.

[40] L. Oggiano, K. Boorsma, G. Schepers and M. Kloosterman, "Comparison of simulations on the NewMexico rotor operating in pitch fault conditions," *Journal of Physics: Conference Series,* vol. 753, 2016.

[41] I. E. Barton, "Comparison of SIMPLE-and PISO-type algorithms for transient flows," *International Journal for numerical methods in fluids,* vol. 26, no. 4, pp. 459--483, 1998.